A Review of ore smelting in High Carbon Ferromanganese production-An induction furnace smelting case study

Keywords: smelting, reduction, manganese, slag, induction

Theresa Coetsee

e-mail: theresa.coetsee@up.ac.za

Department of Materials Science and Metallurgical Engineering, University of Pretoria, South Africa

Abstract

Manganese ore smelting is reviewed in terms of processing parameters such as feed material particle sizes, energy input methods, heat transfer modes, smelting mechanisms, experimental findings on specific smelting aspects and rates of MnO reduction and carbon dissolution into ferrous alloys. This paper provides a comprehensive current review of our fundamental understanding of manganese ore smelting. Process aspects are discussed in terms of existing industrial smelting processes, the SAF (Submerged Arc Furnace) and the BF (Blast Furnace), and compared to an induction furnace smelting case study, the AlloyStream process. Bench scale experimental results for AlloyStream induction furnace smelting are discussed with reference to rate measurements reported in literature. The experimental results clearly illustrate the importance of higher alloy bath temperatures in induction smelting to improve alloy production rates, whilst the effect of alloy bath chemistry was of less importance. AlloySteam process benefits and issues are discussed with reference to the SAF and BF processes.

1. Introduction

Manganese ore smelting is used to produce high carbon ferromanganese from metallurgical grade manganese ore (38-55% Mn). The furnace feed mixture must contain a minimum level of Mn/Fe to ensure that the tapped HCFeMn alloy is on grade as per standard specifications. For example, to produce 78%Mn HCFeMn (Table 1) the ore feed Mn/Fe ratio must be a minimum of 7.5 (Wellbeloved et al., 1990). Usually two or more ores are used as feed material to target the required Mn/Fe ratio, since ores vary in their Mn/Fe values. Ore phosphorus content is an important composition parameter in ore selection because most of the phosphorus in the feed mixture is reduced to the alloy (Olsen et al., 2007), whilst standard alloy compositions specify maximum phosphorus levels, see Table 1.

The bulk of Metallurgical grade manganese ore reserves are found in a few countries: South Africa, Australia, Gabon and Brazil. The Kalahari Manganese Field (KMF) in South Africa is the largest land based manganese ore deposit, containing 74% of known global manganese resources (USGS, 2019). The main South African manganese ores fall into two groups, carbonate containing ore (Mamatwan-type) such as Mamatwan or Gloria ore mined at different mines, but from the same ore body, and high manganese and iron-containing ores (Wessels-type) such as Wessels or Nchwaning ore, (Kleyenstüber, 1984; Chetty and Gutzmer. 2018). Both China and India have large reserves of

ferruginous ores (10%Mn-35%Mn) and produce the bulk of the world's manganese alloys since its primary use is as alloy addition in steelmaking which is dominated by Chinese and Indian steel production plants. World ferromanganese alloys production in 2017 included 4 179 Mt HCFeMn and 13 819 Mt silico-manganese (SiMn). China's production share was 37% HCFeMn and 62% SiMn and India's production share was 12% HCFeMn and 14% SiMn (IMnI, 2018).

The bulk of industrial scale HCFeMn production is done in SAF (Submerged Arc Furnace) plants, with production generated from BF (Blast Furnace) technology in mostly China, but also some plants in Russia and one plant in Japan (Xiaoxing and Daolin, 1998; Pochart et al., 2007; Masukawa and Shiota, 2007; Senin et al., 2018). BF based production in China is particular to processing of their low Mn content ferruginous ores. For example, some ores which contain high levels of Zn, P, Pb, Ag and silica are used to produce high Mn content silica slag for further processing to SiMn (Liu et al., 2019). Double BF processing is also used to smelt high phosphorus containing ferruginous ores to produce pig iron and Mn-enriched slag from the first BF, the slag is then smelted in a second BF with sinter feed materials to produce HCFeMn (Zhang, 1992). The apparent upper limit of power input to a.c. SAF of 100MW has been met already in HCFeMn production (Barcza et al., 2002; Pais et al., 1998). Low furnace burden resistance relative to power supply circuit reactance is the main reason for this upper limit in a.c. SAF electrical energy input. The result is low power factors with larger furnaces at low power factors of~0.53 at 75 to 102MW relative to smaller furnaces of ~0.82 at 18MW (Gericke et al., 1983; Pais et al., 1998). The maximum published hourly production rate from a SAF is 18.4t/h (Pais, et al., 1998) when only sinter feed as manganese source, compared to a BF production rate of 21.9t/h (Kozhemyachenko et al., 1987). Scale-up of the BF is limited by heat distribution and burden materials strength (Takahashi, 2015).

Due to large amounts of expensive coke used as fuel source and reductant in the BF, production cost for BF processing is higher than that of the SAF. One exception was noted by Wellbeloved et al., 1990: in this plant the BF off gas was used to generate electricity for sale. Higher levels of manganese recovery to the alloy is obtained in the BF (75%-91%) compared to the SAF at 74%-79% (Wellbeloved et al., 1990; Kamei et al., 1993). This difference is in part due to higher basicity slags used in the BF compared to slag basicities in the SAF. Lowered loss of MnO to the slag is ensured at higher basicity levels since the activity coefficient of MnO in the slag increases with increased basicity. Also, longer carbon-slag contact time at smelting temperature in the BF, compared to that in the SAF, enables equilibrium or close to equilibrium conditions to be attained in the BF. Higher silicon content in BF produced alloy, compared to SAF produced alloy, illustrate more reducing conditions in the BF smelting process. It is well documented that slag-alloy-gas equilibrium is not attained in the SAF (Ostrovski et al., 2013). Some process development efforts were made to reduce coking coal consumption in BF-type processing by substituting part of the coking coal feed by non-coking coal. Kamei et al. (1993) reported on demonstration plant trials for a shaft furnace of reduced burden height compared to the BF. Non-coking coal (34% volatile matter) was used for heat generation purposes at the tuyeres, similar to PCI (pulverised coal injection) commonly used in the iron BF. The lower burden height of the shaft furnace allows for the use of less coking coal.

Alternative smelting technologies to the SAF and BF were developed to pilot plant and/or demonstration plant scale: DC-arc furnace smelting of manganese ore fines (Schoukens and Curr, 1985), BHPR-NL process for direct reduction of ore fines in a fluidised bed reactor linked to a DC-arc furnace (Crawford, 1995) and the AlloyStream process which combines induction furnace smelting

and fossil-fuel based heating and smelting in one vessel (Coetsee et al., 2015b). DC-arc furnace smelting of ferromanganese ore was abandoned due to excessive manganese vapour losses from the high temperature open bath inherent in the process design (Jones et al., 1993). Large quantities of ore fines (-6mm) are generated in manganese ore mining and mineral processing. The fines generation rate is 30%-70% of the mined ore total (Jones et al., 1993; Gasik, 2013). The use of unagglomerated manganese ore fines feed to the furnace is one of the main points of motivation in the development of alternative smelting processes to the SAF which requires lump ore feed to the larger closed furnaces to maintain gas permeability throughout the furnace feed materials height.

The AlloyStream process was originally developed to produce steel directly from mixed feed of iron ore, coal and fluxes, as described in U.S. patent 6146437 (Fourie, 2000). The process consisted of feeding -10 mm raw material mixture through the furnace combustion zone (freeboard) onto a liquid alloy bath, forming heaps of reacted material; the heap material is heated at the heap top surface by heat generated from burning combustibles with oxygen enriched air in the freeboard. The combustibles consist of fuel gas, coal volatiles, coal carbon and reduction reaction product gas emanating from the heaps. Final reaction and smelting of the heap material is supported by energy transferred from the induction-heated alloy bath. The cross section diagram in Figure 1 illustrates the furnace processing zones.

The AlloyStream process was extensively tested in pilot plant and demonstration plant trials (Coetsee et al*.,* 2015a). Two demonstration plant campaigns were completed, producing 2077 tons HCFeM in the first campaign of 7 months duration and 5014 tons HCFeMn in the second campaign of 11 months duration. The objective of this review is to integrate insights from literature on smelting of manganese ores and to compare its application to the specific case of induction smelting as applied in the AlloyStream process. The latter is presented in the format of bench scale induction furnace simulation experiments conducted to improve process knowledge and understanding as applied to HCFeMn production in the AlloyStream demonstration plant. The importance of these experiments is that they present a reasonably accurate simulation of the induction heated part of the AlloyStream process which is uniquely different in terms of heat transfer mechanisms as compared to existing industrial HCFeMn production processes and alternatively developed processes.

2. Feed material quality and particle size

Gas permeability through the furnace burden must be maintained in both the BF and SAF to prevent furnace eruptions. Therefore the lower limit of feed material particle size to the BF and SAF is 5-6 mm diameter (Wellbeloved et al., 1990). The upper size limit for raw material feed is 30 mm to the BF and 75 mm to the SAF (Wellbeloved et al., 1990; Pochart et al., 2007). In addition, the large burden height in the BF requires high quality coke to maintain gas permeability. Much less high strength coke is required as part of the reductant feed to the SAF due to its lesser burden height (Kamalpour and Rankin, 2004). However, an additional critical factor in SAF carbon source feed materials is its role in setting coke bed resistivity for efficient electrical energy input from the SAF electrodes to the coke bed. In some South African operations as much as 70%-90% of the furnace carbon requirement is supplied as bituminous coal (Wellbeloved, 1990; Wellbeloved and Kemink,

1995). The main disadvantage is the requirement of additional specialised plant equipment to treat organic compounds in the furnace off-gas system due to this coal usage (Wellbeloved and Kemink, 1995).

Briquetting is used to agglomerate manganese-bearing waste for use as a feed stream into the SAF, whilst ore pelletising is avoided due to high costs associated with high firing temperatures required to produce strong manganese ore pellets and the cost of prior fine grinding of the ore (Olsen et al., 2007). A portion of the tapped alloy is entrained in slag and this stream of mixed alloy and slag is returned into the SAF feed as remelts to increase furnace production (Tangstad et al., 2015).

Sintering of the ore in a sinter strand is preferred if a large part of the ore feed contains carbonates so that the electrical energy consumption in the SAF is minimised and also for safe operation by negating furnace eruptions from sudden gas release due to carbonate calcining reactions (Potgieter, 1980; Gericke, 1989). Sintering also allows for the use of ore fines within a specific particle size range (1-9 mm), instead of lump ore only (Gordon and Nell, 2013). Some examples of industrial plant use of sinter as the major part of the furnace feed (70%-100% sinter in the ore feed mixture) have been reported for both SAF and BF furnaces (Pais et al., 1998; Xiaoxing and Daolin, 1998). However, because the reduction of higher oxides of manganese (MnO_2, Mn_2O_3 and Mn_3O_4) to MnO is exothermic, feeding sinter produced from ores containing a high level of especially MnO_2 is not beneficial to the overall furnace mass balance (Tangstad et al., 2015).

In contrast, the AlloyStream process feed consisted of -10mm feed mixture of relatively inexpensive coal, fluxes and manganese ore. Recycling of HCFeMn alloy fines as part of the feed mixture was demonstrated in trials with successful operation at 8% HCFeMn alloy fines in the feed mixture (Coetsee et al., 2015a).

3. Energy input methods, heat transfer modes and smelting

The SAF process applies resistive heating by current flowing through the slag and coke mixture volume beneath the electrodes, referred to as the the coke bed zone (Lee and Tangstad, 2010). Slag conductivity is an important parameter in the heating mechanism of the SAF, with low conductivity preferred (Urquhart, 1980). It has been shown that manganese slag conductivity increases with increased basicity (Woollacott et al., 1974). In contrast, because of the different heating methods in the AlloyStream process the slag composition is not constrained by electrical conductivity. In the AlloyStream process the bulk of the process energy requirement is transferred as radiative heat from the furnace combustion zone (60%-70%) to the upper surface of the solids bed and the slag pool, and the rest of the process energy is transferred to the bottom of the heaps and the slag pool via the alloy bath which is heated by induction (Coetsee et al., 2015a). In both the SAF and the BF efficient convection heat exchange is attained between the hot upward flowing gasses from the main smelting zone in the furnace and the descending materials charge along the vertical height of the furnace materials content. Although the heat so transferred in the BF is generated from combustion in the tuyere zone, as compared to localised resistive heating in the SAF, the overall heat transfer and production efficiency in the BF is unrivalled.

Slag formation also affects furnace burden electrical behaviour. In the SAF the electric resistance of the furnace charge determines operational stability. The specific conductivity of the ore relative to that of the coke in the mixed burden increases with increasing temperature as the ore softens and melts because the contact area between the molten oxide and electrodes increases and also because the ore becomes an ionic conductor as it melts (Miyauchi et al., 2001). Thus, the melting behaviour of the ore is also important for efficient energy input into the ore-coke charge, with ores melting at lower temperature and forming larger quantities of liquid silicate phase being detrimental to stable furnace operation (Miyauchi et al., 2001).

The complexity in electrical energy input in the SAF coke bed due to ore melting behaviour at temperatures of 1250°C to 1600°C was illustrated by Ringdalen et al., 2015. Since silicate containing ores are usually semi-molten already at the onset of MnO reduction to Mn, the complexity of ore melting behaviour stems from not only ore melting, but also from ore smelting behaviour (reduction of MnO and melting of alloy and oxides in the reducing ore). The authors showed a linear correlation between the temperature at which the ore attained 50% reduction in a bulk smelting experiment of a coke-ore mixture placed on top of a coke bed, and the initial ore melting temperature measured in ore placed on a graphite substrate in a sessile drop experiment under CO gas. The main conclusion was that ores with lower melting points reduced at a faster rate than ores with high melting points and therefore liquid phase formation in the ore is the limiting factor in the overall smelting process and not the reduction reaction of MnO from the liquid phase. However, the conclusion requires some qualification since MnO reduction from the liquid oxide requires close contact of this phase to carbon reductant and this close contact between molten ore and carbon is facilitated, and the phase interface readily renewed, if the ore is of low melting point. Also, as discussed above, in the SAF energy input into the coke bed volume is also dependent on slag conductivity and melting ore conductivity which change with MnO reduction extent and assimilation of fluxes into the molten oxide phase (Ringdalen et al., 2015).

A further complicating factor in overall reduction rates discussed by the authors is the viscosity of the molten/semi-molten ore. The viscosity of this phase must not be too low so that the molten/semi-molten ore drains through the coke bed too quickly for the MnO reduction reaction to proceed significantly due to reduced contact time between the liquid phase and reductant carbon (Gaal et al., 2007; Ringdalen et al., 2015). Since the semi-molten ore mostly contains a mixture of silicate liquid phase and solid MnO particles, the effective viscosity of the semi-molten liquid oxide phase will behave as an emulsion with an exponential increase in effective viscosity with increased solid particle (MnO) content (Roscoe, 1952; Tangstad and Olsen, 1997). Feeding ore of low viscosity liquid oxide formation is more suitable for processing in a BF due to its larger coke bed height, as compared to the SAF process which has a much lower coke bed height (Urquhart, 1980). Thus, the multiple factors of ore melting behaviour, MnO reduction rates and resistive heating in the SAF are interdependent factors which are not easily separated from each other in their operational effects in manganese ore smelting.

The bulk of the process energy in the BF is generated by carbon combustion and the rest of the process energy input is gained from heat contained in the hot blast. The overall heat balance is improved by utilising oxygen enriched air and hot blast to increase the combustion flame temperature at the tuyeres, and thus heat transfer to the furnace burden (Kamei et al., 1993; Takahashi et al., 2015). The coke rate can be reduced by using alternative carbon sources for

combustion, for example pulverised fuel injection (Kamei et al., 1993) or heavy oil injection (Masukawa and Shiota, 2007). The bulk of the process energy requirement in the AlloyStream process is generated from combustion of fuel gas, coal volatiles, coal carbon and heaps gas generated from reduction reactions. However, heat transfer efficiency in the AlloyStream is much less than that in the BF because there is limited contact time between feed materials and combustion gasses. The bulk of heat transfer from the combustion zone to the heap surface and slag pool surface is by radiative heat transfer, similar to an open-hearth furnace heat transfer set-up. The result is that a large quantity of heat is retained in the fully combusted off-gas, and this heat should be recovered to ensure financial viability of the plant.

The main process feature differences between the SAF, BF and the AlloyStream process are summarised in Table 2. The main benefits of using the AlloyStream process is the ability to process fine materials (-10 mm) in the form ore ore, coal, fluxes and returned metal fines, directly without agglomeration; use of large proportions of carbonate ore without prior sintering since furnace eruptions is negated via the slag pool; most of the process energy is supplied in situ from combustion instead of outside electricity supply. The latter point is only beneficial in countries which have under developed electricity supply infrastructure and/or expensive coal based electricity supply.

4. Smelting mechanisms

Manganese ore smelting mechanisms are usually studied at laboratory scale and bench scale experiments and sometimes in pilot plant scale tests. However, few detailed pilot plant studies contained in situ measurements. Our understanding of smelting mechanisms in production furnaces is largely based on a few post mortem analyses from production furnace dig-outs following shutdown, (Barcza et al., 1979; Koursaris and Finn, 1985; Olsen and Tangstad, 2004) and a larger number of laboratory and bench scale experiments conducted to measure aspects of smelting mechanisms in general, or in some instances to measure the effect of specific process attributes on smelting mechanisms.

Therefore, interpretation of existing studies as it applies to a different furnace configuration to the SAF requires some additional experimental work as illustrated for AlloyStream in this text. In the AlloyStream pilot and demonstration furnaces the inspection doors at heap level provided ease of access to the furnace interior to collect samples of reacted material from the furnace under normal operating conditions. These samples allowed for much insight into the smelting mechanisms present in the AlloyStream process (Coetsee et al., 2015b).

Processing zones in the SAF have been identified from various dig-outs of industrial and pilot-plant furnaces (Barcza et al., 1979; Olsen et al., 2007). These studies are in agreement that the upper part of the coke bed close to the electrodes, where maximum heat input takes place, is also the main smelting zone. Also, coke is present throughout the slag layer thickness, down to the metal bath level. The top 5cm of the coke bed was identified as the main reduction smelting zone by Olsen et al. (2007). Total coke bed height in the excavated industrial furnace was 250cm, and the slag layer beneath the coke bed was one meter in height (Barcza et al., 1979). Olsen et al. (2007) explained the importance of maximising the contact area between coke and slag to accelerate the reduction rate

of MnO and the factors which will influence coke-slag contact area: slag formation temperature, which in turn is dependent on the type of minerals and their distribution in the particular ore (ore of finely distributed small mineral grains will melt at a different temperature to ore containing large and unevenly distributed grains, thus mineralogy of the ore), slag viscosity, which is also influenced by MnO reduction since the level of MnO in the slag may exceed the MnO saturation level of a particular slag chemistry and so increase the slag viscosity because MnO is then present as a second phase of solid particles in the slag.

Slag-coke bed interaction in the SAF is analogous to slag-coke bed interaction in the BF coke bed (dead man zone), the dripping temperature of the slag and/or the reduced ore mass sets the contact time between it and the coke bed (Ostrovski, et al., 2001, 2002). The authors used a kinetic model to calculate the reduction time required to lower the level of MnO in the furnace charge to that of the tapped slag for both a BF (9%MnO, B=1.5) and SAF (35%MnO, B=0.72), B=(%CaO+%MgO) /(%Al_2O_3+%SiO_2). The calculation results were 334 minutes reduction time required in the BF at 1550°C compared to 55 to 70 minutes at 1500°C in the SAF for coke to ore ratios in the coke bed of 2:1 and 1:1, respectively. The authors conclude that the %MnO in the tapped slag of the SAF is not the same as the %MnO in the coke bed, with the coke bed %MnO being much lower than the tapped slag %MnO. This is an important conclusion, because it may indicate that the temperature at the top of the coke bed, close to the electrodes where the main smelting zone is in the SAF operates, is at much higher temperatures than previously assumed and therefore the heart of the SAF is in fact a very high intensity, small volume reduction zone below the electrodes, and therefore the reduction rates in this zone is much higher than previously anticipated.

Comparison of plant data and equilibrium calculations have shown that slag-alloy-gas equilibrium is not attained in the SAF production of HCFMn, although the slag phase is at equilibrium in terms of its phase composition at high temperatures (Ostrovski et and Swinbourne, 2013). Based on the equilibrium calculations and laboratory experimental results (Yastreboff et al., 2003; Safarian et al., 2008; Sun et al., 2010) the authors concluded that MnO reduction from the slag phase is under mixed control of MnO diffusion in the slag and chemical reaction control (MnO dissolved in the slag reduced by carbon reductant). Similar thermodynamic calculations on AlloyStream pilot plant data confirmed that slag-alloy equilibrium was not attained, although internal slag oxide phase equilibrium was attained (Coetsee et al., 2017).

4.1. Laboratory experiments

Laboratory experiments are usually generic in nature and use small particle size materials (<1mm) because of the relatively small feed sample volume and heating capacity in laboratory furnaces. Therefore, the smelting process information gained from these experiments is usually useful in comparison of ore smelting behaviours among different ore types as focused on the microscopic level, and not with respect to particular furnace process configuration aspects such as particle size, heat input mode, heat transfer mechanisms.

In previous laboratory studies of this kind the same overall sequence of reduction reactions was identified in various manganese ores of different chemical and mineralogical composition. Two to three distinctive reduction stages were identified in Mamatwan ore, Australian siliceous ore fines

and Wessel ore (Koursaris and See, 1979; Eric and Burucu, 1992; Ostrovski and Webb, 1995; Akdogan and Eric, 1995).

In the rapid first reduction stage the higher oxides of manganese and iron are reduced by CO to MnO and FeO (resulting in approximately 30% reduction). In the markedly slower second stage of reduction metallisation of FeO and MnO starts. Metallisation begins with metallic iron nucleation throughout the reduced ore particle, next to solid monoxide particles within the liquid silicate slag. Eric and Burucu (1992) determined that the second reduction stage spanned the reduction range of 30-60% at 1300°C and 30-70% at 1350°C, for Mamatwan ore reduction. It is evident that relatively low temperatures are required for MnO reduction, even in a high basicity ore such as Mamatwan ore, whilst higher processing temperatures are required to melt the oxide components in the feed mixture to ensure separation of slag and alloy (Coetsee, 2017). Typical industrial furnace tapping temperatures of 1450°C-1500°C were reported (Olsen et al., 2007).

In the third stage, final reduction of MnO by carbon occurs. This stage has the lowest reduction rate (Eric and Burucu, 1992), most likely due to the slow diffusion of Mn^{2+} ions in the monoxide phase, and/or liquid slag phase coating the monoxide phase. In the second and third reduction stages manganese is reduced from the liquid slag phase and from the monoxide solid-solution phase, if the latter is present. In ore of negligible MgO content the monoxide phase contains mostly MnO and the MnO activity in the monoxide phase is close to unity because mostly MnO and MgO is present in the monoxide phase. Once manganese reduction has proceeded to the extent that the monoxide phase is consumed, and only dissolved MnO in the liquid slag phase remains, the reduction reaction slows dramatically as the MnO activity decreases, (Tangstad and Olsen, 1997). The carbon used in stage two and three reduction may be sourced from different phases in the reaction system, for example from the carbon dissolved in the alloy droplets in the reduced ore particle, from solid reductant carbon at the edge of the reduced ore particle or from CO gas generated in the Boudouard reaction (Koursaris et al., 1983; Safarian et al., 2008; Coetsee et. al., 2015b).

Several laboratory studies illustrated the importance of close proximity of carbon reductant to MnO (either as solid monoxide phase in slag or dissolved MnO in slag) to improve MnO reduction rates. For example, Kleyenstüber (1979) placed a 20 mm sized cube of Mamatwan ore in a crucible and used pulverised reductant to cover all sides of the cube. The crucible contents was reacted for one to three hours at temperatures ranging from 1200°C to 1500°C under argon gas atmosphere to simulate reaction conditions in a SAF. Carbide phase areas were only observed at the outer edges of the reduced ore cube, in contact with carbon reductant. Inside the ore cube the metallic phase areas were much smaller and reported as single phase Fe-Mn alloy, not carbides. The general observation from a later mineralogical investigation by Koursaris and Finn (1985) of samples extracted from the furnace dig-out by Barcza et al. (1979) are in agreement with the laboratory study findings of Kleyenstüber (1979). Especially the conclusion made on the formation of Fe-Mn carbide at the surface of ore lumps, but single phase Fe-Mn alloy beads of smaller volume formed inside ore lumps, and thus the importance of ore/slag and carbon proximity in manganese metal formation. Koursaris and Finn (1985) did conclude that direct contact between carbon and ore/slag is not required to form carbide globules at the surface of the sintered lump of ore. These carbide globules were hand-picked and analysed to contain 54 %Mn, 37 %Fe and 5.2 %C.

Since the ore is semi-molten and form a mushy charge as described by Koursaris and Finn (1985), the reaction interfaces of ore/slag with carbon reductant is changing all the time, and this reaction interface shift complicates making conclusions from macro scale observations on the importance of direct contact of ore/slag with carbon. Koursaris and Finn (1985) identified a somewhat different reduction mechanism at lower temperatures when the charge is in this mushy state. It was observed that alloy which formed at the ore-carbon interface eventually enveloped the carbon particle and then this alloy formed the new reduction interface between ore/slag and carbon via carbon dissolved in the alloy.

Carbon dissolved in alloy areas within the reduced ore particle is assumed to be a source of carbon for reduction of MnO in the reduced ore particle interior. Once the reduced ore particle is sufficiently molten to encapsulate interior alloy areas, there is no contact between these alloy areas and carbon reductant or CO gas at the reduced ore particle surface, and dissolved carbon replenishment is prevented. In this scenario the existing alloy areas may still grow in size from reduction of MnO by carbon dissolved in the alloy areas, but no new alloy areas will form (Ostrovski and Webb, 1995). There are observations which confirm absence of growth of interior alloy areas in partially molten ore reacted at 1400°C (Ostrovski and Webb, 1995), and from industrial furnace samples (Koursaris and Finn, 1985). In comparison, the alloy areas at the surface of the reduced ore particles increased significantly in size. From these observations it seems that reduction of MnO by carbon dissolved in alloy areas interior to the semi-molten reduced ore particle is insignificant.

The effect of close proximity of reductant to MnO was clearly illustrated in a few studies on self reducing pellets (Hofman et al., 1989; Braga et al., 2007). At 1250°C to 1400°C reduction temperatures a final alloy liquid carbide formed in the pellet interior, without bulk melting of the pellet, so avoiding slow metal-slag reactions since MnO reduction proceed quickly before bulk slag formation occurred (Braga et al., 2007). The importance of reductant proximity was clearly explained by Rankin and Wynnycki (1997) in considering experimental results in the prior work of Rankin and Van Deventer (1980) in which pure MnO-graphite mixtures reacted at 1250°C to 1425°C. The authors used modelling to show that the rate controlling step in most of the MnO-graphite reduction experiments was intrinsic transport of CO_2 from MnO particle surfaces to the carbon reductant surface, and not the Boudouard reaction as previously thought.

Rankin and Van Deventer (1980) and Van Deventer (1987) showed that the addition of even a small quantity of silica to pure MnO (2.5 mass%) caused a lowered reduction rate of MnO with graphite at 1350°C due to formation of molten ß-$MnSiO_3$. Most of the metallurgical grade ores contain silica gangue which tends to react with MnO to form low temperature molten phases of $2MnO.SiO_2$ or $MnO.SiO_2$ initially, with incorporation of other gangue oxides such as CaO, MgO and Al_2O_3 as permitted by mineralogy factors (Kleyenstüber, 1979; Eric and Burucu, 1992; Akdogan and Eric, 1995; Ostrovski and Webb, 1995; Visser et al. 2013; Ringdalen et al., 2015; Coetsee, 2019). Therefore, as compared to reduction of pure MnO, the MnO in ore is encapsulated by a silicate slag layer, so adding another diffusion barrier to the reduction reaction sequence. Intrinsic transport of CO_2 may not be rate limiting in this reaction set-up. Yastreboff et al. (2003) concluded that reduction of MnO dissolved in silicate slag was under mixed control of CO mass transfer in the gas phase and the chemical reduction reaction. However, Safarian et al. (2008) used thermodynamic calculations to show that the observed effect of CO in the experiments of Yastreboff et al. (2003) was a result of a shift in the equilibrium activity of MnO, and not due to the diffusivity of CO in the gas phase.

The main reduction rate model used for MnO reduction from slag is based on the overall reaction of MnO with solid carbon because this reaction is assumed to be rate controlling (Olso et al., 1998; Yastreboff et al., 1998; Ostrovski et al., 2001, 2002; Safarian and Kolbeinsen, 2008). Use of this rate expression is convenient and does not imply that reduction via CO is ignored. The work of Rankin and Wynnycki (1997) and Safarian et al. (2008) showed that CO gas reduction of MnO is important in the overall reduction process.

5. Kinetics

de Oliveira et al. (1999) measured the rate of graphite carbon dissolution into iron containing 5%Mn and 15%Mn, respectively and 0%C initially, at 1600°C in an induction furnace and under argon gas atmosphere. The authors assumed mass transfer control for the carbon dissolution reaction and found that the mass transfer equation described their alloy bath carbon content measurements well. Mass transfer coefficients of 5.180 x 10^{-2} cm/s and 7.639 x 10^{-2} cm/s were measured for iron containing alloys of 5%Mn and 15%Mn, respectively. The authors explained that an increased graphite dissolution rate with increased alloy manganese content was due to both the increased driving force for dissolution due to the difference in carbon saturation level at the experimental temperature and the increase in the mass transfer coefficient. In a separate induction furnace experiment in the same study the reduction rate of MnO from FeO-MnO-SiO_2 slag by carbon saturated Fe-Mn alloy contained in a graphite crucible was measured at 1600°C under argon gas atmosphere. FeO was quickly reduced at the start of the experiment, resulting in a MnO-SiO_2 slag forming. Slag samples were collected over time and subsequently analysed for %MnO remaining. The authors concluded that the rate of carbon dissolution into Fe-Mn alloys is faster than the rate of reduction of MnO by carbon saturated Fe-Mn alloy. The initial rates of carbon dissolution and MnO reduction from de Oliveira et al. (1999) were reworked to comparable units as illustrated in Table 3 by using the stated alloy volume (38.22cm^3) and alloy-graphite crucible contact area (25.64cm^2) in the carbon dissolution experiments with Fe-Mn alloy density data from Lee et al. (2011).

Skjervheim and Olsen (1995) showed that mechanical stirring of the slag and alloy (carbon saturated manganese) did not affect the MnO reduction rate, and therefore diffusion is not the rate controlling step in this reaction system. In a separate set of experiments of slag and alloy (carbon saturated manganese) contained in graphite crucibles, Skjervheim and Olsen (1995) showed that the MnO reduction rate at the slag/graphite interface was 2.3 times larger than that at the slag/metal interface. In the latter experiment reduction of slag due to contact with the graphite crucible wall was prevented by inserting a molybdenum sheet between the slag and the crucible wall.

From the rate values of de Oliveira et al. (1999) as illustrated in Table 3 it is seen that the carbon dissolution rate is two orders of magnitude larger than the reduction rate from carbon dissolved in the alloy. Therefore, given similar reaction interface area values for these two reactions, the alloy bath should stay saturated even if MnO reduction from dissolved alloy carbon takes place. In addition, the work of Skjervheim and Olsen (1995) confirms that the importance of MnO reduction by carbon dissolved in alloy is of less importance compared to MnO reduction by solid carbon reductant.

Table 4 summarises reduction rates of MnO from slag from different studies. In all these studies the reduction reaction for MnO by carbon reductant (as solid carbon or carbon dissolved in alloy) was considered to be under chemical reaction control. The following rate equation was used to express reaction rates for the reduction of MnO by solid carbon reductant:

$(MnO) + <C> = (Mn)_m + [CO]$ (1)

$Rate = kA(a_{MnO} - a_{MnO(eq)})$ (2)

( ) = liquid; < > = solid; $( )_m$ = dissolved in alloy; [ ]=gas

Rate = MnO reduction rate in g. MnO/min/cm^2

A=carbon-slag reduction reaction interface area (cm^2)

a_{MnO}=activity of MnO in slag

$a_{MnO(eq)}$=equilibrium activity of MnO in slag

The MnO reduction rate values reported by de Oliveira et al. (1999) were reworked to the values displayed in Table 4 to ensure comparative units with the reported values from Olso et al. (1998) and Ostrovski et al. (2001) in values in g. MnO/minute/cm^2. The numbers presented in Table 4 for the studies by Olso et al. (1998) and Ostrovski et al. (2001, 2002) are the values of R/A from the rate expression in (2) since the value of the reaction interface area between carbon and slag were not explicitly stated. The activity of MnO in the slag was assumed to be one and the equilibrium activity of MnO is small since the experiments were done under argon gas. The values reported in Ostrovski et al. (2001, 2002) were calculated in their study from prior experiments done by the authors at 1250°C to 1400°C (Yastreboff et al., 1998). The values reported in Table 4 from the work of Safarian and Kolbeinsen (2008) are for the highest rates achieved with one of six graphite types and are mostly slower than those reported in the other studies. The reason for the slower rates is that the slag was single phase only and therefore the MnO activity values were not taken as one in the rate expression. The calculated MnO activity values (using FactSage 6.4) for the starting slag composition used by Safarian and Kolbeinsen (2008) was used in the rate expression to attain the values for this study as reported in Table 4 are: 0.278 at 1450°C, 0.292 at 1500°C and 0.319 at 1600°C.

Xu et al. (1993) studied the reduction of MnO from FeO-MnO-SiO_2-CaO slag by carbon saturated liquid iron at 1580°C with and without additional reductant coke added into the slag. The iron alloys contained different levels of manganese (0%Mn, 10%Mn and 30%Mn). MnO reduction was considered to via Fe in the alloy:

$(MnO) + (Fe)_m = (FeO) + (Mn)_m$ (3)

$(FeO) + [CO] = (Fe)_m + [CO_2]$ (4)

$[CO_2] + <C> = 2[CO]$ (5)

( ) = liquid; < > = solid; $( )_m$ = dissolved in alloy; [ ]=gas

From modelling of the rate data the authors concluded that the first reaction (reaction (3)) in the sequence of proposed reactions was the slowest if no coke reductant is added into the slag. The

authors did not report on the reduction interface areas and therefore sensible rate comparison to the numbers reported from other studies is not possible.

Several studies were done on the dissolution rate of different carbon types into iron metal because this reaction is important in iron ore smelting process such as the HIsmelt process (Cusack et al., 1995). Most of these studies concluded that liquid-side mass transfer controls the dissolution of carbon into the alloy. The rate expression used and its variables are as follows:

$$\frac{dC}{dt} = \frac{kA}{V}(C_s - C_t) \quad (6)$$

k=mass transfer coefficient (cm/s)

A=dissolution interface area (cm^2)

V=molten alloy bath volume (cm^3)

C_s=mass% carbon in the alloy at carbon saturation

C_t=alloy bath carbon content (mass%) at time (t)

The overall carbon dissolution rate constant K (1/s) is defined as kA/V to simplify equation (6) for comparison of rates among different studies.

Wu and Sahajwalla (2000) measured the dissolution rates of various coals and graphite into iron melts at 1550°C. Dissolution rates of synthetic and natural graphite were significantly faster than the dissolution rates of five coals. The graphite dissolution rate constant was unaffected by initial iron bath carbon content, but the coal dissolution rate constant decreased with increased initial iron bath carbon content. The layer of carbon fed onto the induction heated alloy bath was of narrow particle size range (1.18 mm to 2.32 mm). The overall carbon dissolution rate constant (K) is used to compare measured dissolution rates from different studies because the exact carbon-alloy interface area is not certain in when nongraphitic carbon is used (Wu and Sahajwalla, 2000). Since de Oliveira et al. (1999) stated the alloy volume and dissolution interface area in their experiments on graphite dissolution the mass transfer coefficient (cm/s) can be translated to a value of K (1/s) for comparison purposes in Table 5.

Jang et al. (2012) measured the dissolution rates of coke into iron at temperatures of 1450°C to 1650°C. The authors showed that the rate controlling step in carbon dissolution from coke changed from liquid side mass transfer to chemical reaction control at 1450°C due to initial slag formation at the carbon-alloy interface resulting in a decrease in dissolution interface area and dissolution rate. At increased temperatures, the slag layer became more fluid and could be removed from the dissolution interface to increase the carbon-alloy interface area again. At 1550°C the dissolution process was under mixed control (chemical reaction and liquid side mass transfer) and at 1650°C the dissolution process was under complete mass transfer control. In the case of graphite dissolution at temperatures of 1300°C to 1650°C, mass transfer control prevailed since no significant ash layer formed at the graphite-alloy interface. Both studies, Wu and Sahajwalla (2000) and Jang et al. (2012), pointed out that carbon dissolution rates from graphite is generally higher than carbon dissolution rates from nongraphitic carbons such as coal and coke. Apparent rate constant values

from these studies as displayed in Table 5 and Figure 3 illustrate this point as well. The highest values are those for graphite dissolution in manganese containing alloys (de Oliveira et al., 1999).

It is already well known that variations carbon dissolution rates into iron based alloys is carbon type dependant. However, the effect of different carbon types on the rate of reduction of MnO from slags is not that clear. Gaal et al. (2004) found carbon type to influence MnO reduction rates with eucalyptus charcoal forming more metal per mass unit of carbon, compared to anthracite and coke. Reduction rate differences were were not as large for MnO reduction from slag as for SiO_2 reduction from slag. Safarian and Kolbeinsen (2008) found the effect of temperature more important than carbon properties among different types of graphite tested. Safarian et al. (2008) confirmed that eucalyptus charcoal reduced MnO faster than cokes, whilst industrial coke showed faster reduction rates than coke produced from a single coal. Cokes with higher surface area and crystallite size (industrial cokes) showed higher MnO reduction rates. No clear relation could be shown between reductant CO_2 reactivity of reductant and its slag-reactivity (MnO reduction rate). However, if the slag contains significant quantities of FeO (10%), the overall slag reduction rate by coke was faster than for eucalyptus charcoal, and both coke and eucalyptus charcoal showed much faster reduction rates than graphite (Safarian et al., 2009). Clearly, the importance of carbon type is linked to the predominant reduction mechanism or combination of mechanisms of MnO reduction: direct reduction of MnO by carbon, reduction via CO gas, or reduction via carbon dissolved in the alloy, or as in the latter study on high FeO slags, reduction of MnO by Fe in the alloy in combination with CO gas reduction of FeO.

Even though the rate equation for MnO reduction is expressed in terms of solid carbon as reductant, and it is generally acknowledged that carbon dissolved in alloy may be an important contributor as MnO reductant. However, the reaction interface area from these two reaction sites is limited as compared to that available to CO gas. Safarian et al. (2008) showed that the overall MnO reduction rate from slag is much higher under CO gas, in the presence of solid carbon reductant, compared to the same reduction experiment under argon gas, even though the reaction rate constant for MnO reduction by carbon is four times larger than that for MnO reduction by CO gas. The reason for the differences in overall MnO reduction rate and reduction rate constant is the effect of the much larger slag-CO gas interface area, which was ten times that of the slag-carbon interface area. These results highlight the benefit of MnO reduction by CO gas: the reaction interface area is increased by orders of magnitude as compared to the size of the reaction interface area if only ore/slag-carbon contact area is the MnO reduction reaction interface area.

The minimum temperature required to reduce MnO by CO gas in the presence of solid carbon is set by the values of manganese activity in the alloy and MnO activity in the slag (Braga et al., 2007; Safarian et al., 2008). When reduction via CO gas is enabled, the reduction mechanisms are similar to that of iron ore reduction via CO gas, with regeneration of CO_2 in the Boudouard reaction. This minimum temperature can be as low as 1250°C (Coetsee, 2018).

The current study is focussed on reduction stages two and three (reduction of MnO), as applied in the induction heated configuration of the AlloyStream process. Induction heating has been used in a few manganese ore reduction studies (Koursaris and See, 1979; Gaal et. al., 2004). Koursaris and See (1979) used an induction furnace set-up in to simulate the SAF process. This set-up was configured to heat the whole feed mass in the absence of an initial alloy bath. In contrast, the experimental set-

up used in the current work ensured heat transfer from the induction heated alloy bath to the layer of feed material placed on top of the alloy bath (the alloy bath was first melted and then the feed mixture material was fed onto the alloy bath). The layered heat transfer set-up was important to ensure that the experiments closely simulated the induction heating configuration which is specific to the AlloyStream process. Gaal et. al. (2004) used induction heating to heat bulk slag contained in a graphite crucible. This use of induction heating was not of particular importance, but rather a matter of convenience.

6. Induction furnace smelting experiments

6.1. Raw materials

Feed material consisted of a mixture of pre-reduced manganese ore (-6.3 mm), Eikeboom char (-2 mm) and burnt dolomite flux (-2 mm). The manganese ore contained the following major mineral phases: pyrolusite (MnO_2), goethite (FeO(OH)) and quarts (SiO_2). The ore was pre-reduced to MnO at 1000°C furnace temperature in a CO gas atmosphere. Sample mass loss measurement and XRD analyses were sued to verify the reduced ore reduction extent. Coal was charred under N_2 atmosphere at 1000°C. Dolomite was calcined at 1000°C in an air atmosphere. The use of a feed mixture of pre-reduced ore to MnO level, charred coal and calcined dolomite flux as feed materials to the smelting experiments was informed by prior separate simulation experiments which confirmed that the feed mixture at the top surface of the heap (see Figure 1) was at least reacted to complete calcination of dolomite and reduced to MnO. This was also confirmed from heap samples taken during pilot plant trials (Coetsee et al., 2015b). Analyses of pre-reduced manganese ore and burnt dolomite are presented in Table 6, and that for Eikeboom char in Table 7. Chemical analyses of pre-reduced ore, char ash and dolomite flux were done by Inductively Coupled Plasma Optical Emission Spectrometry (ICP-OES) method. Alloy carbon content and char ultimate analysis (C, H, N) were done by combustion (LECO) analysis method.

The feed material mixture consisted of 74.8 mass% pre-reduced ore, 17.4 mass% Eikeboom char and 7.8 mass% burnt dolomite with aim slag basicity of values of B2=0.74=(%CaO/%SiO_2) and B3=1.23=(%CaO +%MgO)/%SiO_2. The char addition level to the feed mixture was calculated at 10% excess to the base amount of char required to produce high carbon ferromanganese alloy from the feed mixture. The base carbon amount was calculated by using a mass balance based on the following assumptions: 80% manganese metallisation from MnO, 100% iron metallisation from FeO in the pre-reduced ore and Fe_2O_3 in the char ash, 7.5%C in the expected alloy mass, and the reduction reaction product gas contained CO only. The level of excess carbon added as char is sensibly expressed as the mol ratio of carbon to reducible oxygen (C/O), at the level of 1.23 for the feed mixture used in this study. In the (C/O) ratio calculation the char carbon content as expressed in the ultimate analysis in Table 7 is used, and the reducible oxygen content (O) is calculated as the sum of the oxygen associated with manganese and iron oxides in the feed mixture. The level of dolomite addition was set to protect the MgO crucible refractory material at a bath temperature of 1550°C and at 80% manganese recovery to the alloy.

Table 8 illustrates this target slag analysis. For referencing, the expected slag analyses in the feed mixture at zero and 40% manganese recovery, as well as the initial pre-reduced ore composition, are

presented. Iron oxide is excluded in the compositions in Table 8 since it is quickly reduced to iron metal at the start of the reduction process. Figure 4(a) indicates that solid monoxide phase should be present in the pre-reduced ore at 1550°C at manganese recovery levels up to 65%. Therefore, at 1550°C, along the reduction path illustrated in Figure 4(a), the activity of MnO remains close to unity down to levels of 65% manganese recovery to the alloy. Similarly, high MnO activity is maintained in the whole feed mixture as indicated in Figure 4(b) to 4(d) in the bulk slag at 0% and 40% manganese recovery at 1550°C and at 80% manganese recovery level at approximately 1540°C. The liquidus projection diagrams in Figures 4(a) to 4(d) were calculated from FactSage 6.4 using FToxid database (Bale et. al., 2008).

6.2. Experimental set-up

The experimental set-up (see Figure 5) is based on the set-up developed for similar experiments conducted in iron ore reduction studies (Lourens, 2008). A few modifications were made for use in this work: the dust settling box was modified to allow for sampling of the liquid bath under argon gas during experiments and the mass of the initial alloy bath was chosen to be 5000 grams (instead of 12 kg. used previously) to quantify manganese pick-up in the alloy bath by measurement of the end point alloy bath chemistry.

The crucible was positioned in the furnace induction coil space so that only the alloy bath was heated by induction, and not the whole crucible contents. Precise crucible placement was important to ensure that heat transfered from the alloy bath to the feed mixture (floating on the alloy bath) was the main heat transfer method, and not direct induction heating of any alloy droplets formed within the material feed mixture. Crucibles were made from high MgO castable material. The crucible dimensions were 150 mm inner diameter, 30 mm wall thickness, and 320 mm crucible height. The heating rate of the alloy bath to the target temperature was limited to 3-10°C/minute to maintain crucible integrity.

The alloy bath was initially formed by melting either medium carbon ferromanganese alloy or carbon steel placed into the MgO crucible. The crucible was continuously purged with argon gas to prevent oxidation of the alloy. Once the alloy was molten, coal char was added and the alloy bath stirred to carburise to the aim initial alloy bath level. After collection of a small sample from the initial alloy bath the feed material mixture was added onto the alloy bath (as a single batch) to start the reduction experiment. The initial mass of 5000 grams of alloy was selected to ensure a thin metal bath height of 40 mm which ensured a small initial alloy mass in which the level of manganese increased due to manganese ore reduction could be quantified from chemical analyses.

A substantial supply of argon gas at a flow rate of 5.9-6.9 Nl/min was maintained into the crucible to ensure that a positive pressure was always maintained over the crucible contents, pushing reaction gasses and argon out at the crucible/lid interface, so that air ingress was prevented. The argon gas exit flow from the crucible was pumped to a Prima 600S mass spectrometer to analyse the product gas over the experimental time period. The argon gas was dried, and oxygen removed using an “oxyzorb” cartridge. The product gas analysis was monitored continuously to check that as little as possible air infiltrated the crucible.

Material bed temperatures were measured throughout each experiment at two vertical positions of 30 mm and 10 mm from the alloy bath surface. Stainless steel sheathed K-type thermocouples were used to make these measurements. Alloy bath temperatures were periodically measured by inserting an alumina sheathed S-type thermocouple into the alloy bath. This measurement took several minutes to complete since the alumina sheath was lowered slowly into the heated zone to avoid thermal shock. Therefore an alternative method was periodically used to infer the alloy bath temperature from the temperature differentials measured between two to three S-type thermocouples positioned on the MgO crucible outer surface and the direct alloy bath temperature measured with the alumina sheathed S-type thermocouple. Inductor power was momentarily switched off during S-type thermocouple measurements to prevent induction interference in these measurements.

At the end of the experimental period, a layer of char and a layer of burnt dolomite were added on top of the crucible contents, and then the crucible was removed from the furnace and quenched under air blown by an industrial fan. After the crucible and its contents cooled to room temperature, the crucible content was set in epoxy for vertical sectioning. Metal samples were taken from the solidified metal bath at various positions and combined into one sample to obtain the average end point alloy bath composition.

Four experiments were conducted to measure the effect of alloy bath temperature and alloy bath chemistry on the reduction process. Experimental conditions are summarised in Table 9. The initial alloy bath carburisation levels were selected in order to attain similar liquidus temperatures for the iron and ferromanganese alloy bath chemistries. Thus ensuring similar levels of alloy bath superheat at similar alloy bath temperatures for the same approximate level of carbon in both the iron and the ferromanganese alloys. It was estimated from the Fe-C and Fe-C-Mn available phase diagrams in literature that 3.5%C in the initial alloy would result in liquidus temperatures of 1180°C at 3.5%C for ferromanganese (80%Mn) and 1235°C at 3.5%C for iron (Thornton and Colangelo, 1985; Rivlin, 1984).

Experiment 1 was done to measure the reduction rate over an extended period of time to monitor the possible effect of slag layer formation on production rate. Experiment 2 referenced a shortened reaction period for comparison to experiment 1. The iron bath temperature was lowered in experiment 3 for comparison to experiment 1. Experiment 4 was done for comparison to experiment 3 to test the effect of metal bath composition.

The actual starting alloy carbon content levels were somewhat different from the aim compositions (see Table 9). The actual liquidus temperatures for the initial and final alloys (see Tables 11 and 12) were calculated using FactSage 6.4 thermochemical software, using the SGTE alloy database. The calculation results in Figure 6 illustrates that initial superheat levels in experiments 1 and 4 are similar at 200°C, however the end point superheat levels are much different. The opposite effect holds in experiments 3 and 4, initial superheat levels differ by 100°C, but the difference narrows to 8°C for the end point alloys. Therefore, care should be taken in the interpretation of the possible effects of superheat and alloy bath temperature on the reduction rate achieved in the different experiments. The initial and end-point alloys were fully liquid at the bath temperatures used. This is illustrated in Figure 7 in terms of the alloy carbon saturation levels which are much higher than the carbon levels attained in the experimental alloys.

7. Results and discussion

The product gas analyses and temperature measurements from each experiment are illustrated in Figures 8 to 11. The product gas analyses for experiment 2 is limited to the initial reaction period due to escape of some of the argon purging gas through the unfastened sampling port cap which resulted in insufficient product gas flow into the mass spectrometer. In experiment 1 the CO gas rate stayed at levels of ±20% for about one hour, and then decreased slowly over a period of 30 minutes. Alloy bath temperatures and material bed temperatures remained relatively constant throughout the experiment, leading to the conclusion that reduction rates decreased due to processing effects which developed over time. Slag layer formation at the material mixture/bath interface may be one such effect, interfering with reduction progress.

Because of very low levels of CO_2 required to reduce MnO to Mn, the presence of CO_2 in the product gas analyses is most likely due to subsequent reaction of CO emanating from the material/bath interface, most likely due to initial reduction of FeO to Fe. The two thermocouples inserted into the fed material bed at 10 mm and 30 mm from the liquid alloy bath, measured temperatures of 800-850°C, illustrating the very steep temperature profile in the heat affected material bed layer. Therefore, the reduction reactions occurred only within the relatively thin material bed layer which was heated to sufficient temperatures to drive MnO reduction reactions.

The product gas analyses in Figures 8 to 11 were used to calculate alloy production rates in terms of mass of manganese and iron alloy produced over time. The calculation basis used was that each mole of oxygen in the product gas was the result of a mole of metal (manganese or iron) produced, at 55 gram metal per mole oxygen. The relative production rate time series in Figure 12 shows that the initial rates measured in experiment 2 are in agreement with initial rates measured in experiment 1, confirming repeatability in experimental conditions. Figure 12 clearly shows the importance of alloy bath temperature, and thus heat transfer rate, which is illustrated by doubling in instantaneous production rate in experiments 1 and 2, as compared to experiments 3 and 4, resulting from alloy bath temperatures in experiments 1 and 2 at ±150°C in excess of the alloy bath temperatures in experiments 3 an 4.

7.1. Alloy bath thermodynamics

The similarity in production rates achieved in experiments 3 and 4, indicates that the reduction process is only slightly affected by alloy bath chemistry. The importance of this observation is that it indicates the predominant mechanism in MnO reduction in the process configuration simulated in this study: MnO reduction via reductant contained in the alloy bath is of less importance as compared to MnO reduction within the feed mixture layer floating on top of the alloy bath. The following thermodynamic analysis illustrates the expected effect of carbon and manganese activities in the alloy on the reduction reaction (7) driving force if this reaction was dominant in the overall reduction process. However, as stated above, alloy bath temperature and its effect on heat transfer rate and thus smelting in the heap reaction zone was the dominant reduction mechanism since reduction rates in experiments 3 and 4 were similar and not of large difference which would have been the case if the alloy bath composition dominated the reduction process via reaction (7).

The main MnO reduction reaction at the contact interface of the alloy bath surface and the feed mixture or slag layer is illustrated in reaction (7). As already indicated in Figures 4(a) to 4(d), the activity of MnO remained high throughout the experiments. Although the CO content in the product gas analyses varied over time and among the experiments, a realistic assumption is that the product gas emanating from reaction (7) at the alloy bath surface consisted of CO gas only. Then, in terms of alloy bath chemistry, only the relative activities of C and Mn in the alloy may influence reaction (7) thermodynamics.

$$(MnO) + (C)_m = (Mn)_m + [CO] \quad (7)$$

( ) = liquid; < > = solid; $( )_m$ = dissolved in alloy; [ ]=gas

FactSage 6.4 thermochemical software (using the SGTE alloy database in the equilibrium module) was used to calculate the effect of alloy bath chemistry on the activities of carbon and manganese. The activity values of manganese at 1500°C in Fe-Mn alloy, and in Fe-Mn-C alloy at 3% C and 5% C, are summarised in Figure 13. Iron and manganese form an almost ideal solution. Addition of carbon to the Fe-Mn alloy results in a decrease in manganese activity from 0.61 at 3%C to 0.48 at 5% C. This difference is not large since the alloy is fully liquid at these carbon levels. Low levels of manganese in the initial and final iron bath compositions in experiments 1 to 3 resulted in low manganese activity levels, less than 0.02.

The limited effect of alloy composition on carbon activity is illustrated in Figure 14. Although the effect of manganese content on carbon activity is more pronounced at higher levels of carbon dissolved in the alloy, the relative change in carbon activity values is small since carbon activity levels are low, ranging from a minimum value of 6.9×10^{-4} (Figure 14, point A) in the start ferromanganese alloy bath to a maximum value of 5.6×10^{-3} in iron containing 5%C (Figure 14, point B). Given these thermodynamic trends in activity values, the activity levels in the initial and end point alloys in experiments 3 and 4 were calculated, summarised in Table 10, to quantify the expected effect on thermodynamic driving force in reaction (7). The thermodynamic driving force for reaction (7) is much lower in the case of ferromanganese alloy bath as compared to the iron bath. Therefore, provided thermodynamic driving force is the main determinant in MnO reduction following reaction (7), large differences in reduction rates are expected in experiments 3 and 4 when using iron and ferromanganese alloy bath chemistries, respectively. However, it is clear from Figure 12 that reduction rates in experiments 3 and 4 are similar in magnitude and thus not much affected by alloy bath composition.

7.2. The effect of carbon dissolution into the alloy bath

The rate of carbon dissolution into the alloy is fast compared to alloy formation and melting rates, as indicated from comparison of alloy bath carbon contents at the end of experiments 1 and 2. These values are similar at 4%C (see Table 12), although the duration of experiment 1 was 96 minutes, and that of experiment 2 was 31 minutes.

The relative importance of reactions at the bath-heap interface was investigated by calculating the expected carbon dissolution rate from equation (6), using rate constant values from literature. Rate constant values for graphite dissolution were taken from the work of de Oliveira et al. (1999) for dissolution into 5%Mn-Fe alloy at 1600°C and from the work of Jang et al. (2012) for dissolution into pure iron at 1550°C. The rate constant for the slowest coal carbon dissolution rate into Fe-2%C-0.02%S alloy was taken from the study by Wu and Sahajwalla (2000). Since carbon dissolution rates from nongraphitic carbons are lower than the values for graphite dissolution rates (see Figure 3 for comparison), the calculated curves in Figure 15 represents both the quickest and slowest bath carburisation rates expected if sufficient alloy bath-carbon contact occurred and no carbon refining from the alloy bath occurred, for example from reaction with MnO in the slag. It is seen that the actual end point %C in both experiment 1 at 4.0%C (96 minutes) and experiment 2 at 4.1%C (31 minutes) are well below the expected dissolved carbon level. This indicates a low rate of carbon dissolution into the alloy bath due to insufficient alloy bath-carbon contact. Comparison of the average carbon dissolution rate in experiment 2 to the maximum instantaneous MnO reduction rate from Figure 12 indicates similar values: 2.17 x 10^{-3} mol C/s dissolved vs. 2.42 x 10^{-3} mol MnO/s reduced. However, the rate of MnO reduction levels off over time, yet the level of carbon dissolution did not increase with increased reaction time to 96 minutes, indicating that refining of alloy carbon via MnO reduction was insignificant.

The maximum instantaneous MnO reduction rate in Figure 12 (for experiment 2) is 8.23 x 10^{-4} mol/minute/cm^2 as expressed for the bath cross section area of 176.7cm^2. This MnO reduction rate value is similar in magnitude to the value in Table 3 from in the study by de Oliveira et al. (1999). The relative absence of direct contact of alloy bath with reductant carbon is seen in the polished section in Figure 16. These observations are in agreement with tapped alloy analyses measured in the pilot plant and demonstration plant trials. The tapped HCFeMn alloy analyses from these trials were never at carbon saturation levels, even in the presence of excess carbon in the furnace heaps (Coetsee et al. 2015a, 2017).

7.3. Mass balance calculations

The alloy production numbers calculated from product gas analyses, and illustrated in Figure 12, may be different to the actual amount of alloy melted into the alloy bath. Therefore, mass balance calculations were made to compare alloy production numbers calculated from product gas analyses to that melted into the alloy bath. In experiments 1 to 3, the mass of manganese metal melted into the alloy bath was calculated from the manganese mass balance in equations (8) and (9).

$$M_{Mn} = (M_0 + M_c)(\%Mn_{end} - \%Mn_{start})/100 \quad (8)$$

$$M_c = M_0(\%C_{end} - \%C_{start})/100 \quad (9)$$

M_{Mn} = mass manganese melted into the alloy bath
M_0 = initial carburised alloy bath mass (see Table 9)
M_C = minimum mass of carbon added to alloy bath over reaction time
$\%Mn_{start}$ = mass% Mn in alloy bath at the start of the reaction time

$\%Mn_{end}$ = mass% Mn in alloy bath at the end of the reaction time
$\%C_{start}$ = mass% C in alloy bath at the start of the reaction time
$\%C_{end}$ = mass% C in alloy bath at the end of the reaction time

The mass of iron melted into the alloy bath was calculated based on an estimate that a third of the feed material mixture was sufficiently heat affected to separate alloy from slag to enable melting of the produced alloy into the alloy bath. This is illustrated in the typical cross section in Figure 16 which shows the smelting volume marked between the two black lines drawn onto the photograph. The smelted layer thickness is ±2.5 cm of a total feed material height of ±9.0 cm, which translates to ±28% of the feed material volume smelted. Because the bed temperatures measured in Figures 8-11 are similar (800°C-850°C), the proportion of the heat affected zone (smelting volume) is assumed to be similar in the experiments. Therefore, a third of the iron in the feed mixture (36 grams of 109 grams in the feed mixture) was added to the manganese metal mass number (M_{Mn}) calculated from equations (8) and (9), to provide the mass of Mn and Fe melted into the alloy bath.

In experiment 4, the starting alloy bath consisted of ferromanganese alloy and thus the manganese mass balance could not confidently be used to calculate the mass alloy melted into the bath. The iron mass balance was used to calculate the mass of iron and manganese melted into the alloy bath, using equations (10).

$$(M_{Mn} + M_{Fe}) = \left(M_{Mn}^{end} + M_{Fe}^{end}\right) - M_{Mn}^{start} - M_{Fe}^{start}$$

$$M_{Mn}^{start} = (M_0)(\%Mn_{start})/100$$

$$M_{Fe}^{start} = (M_0)(\%Fe_{start})/100$$

$$(M_{Mn} + M_{Fe}) = \left(M_{Fe}^{start}\right)(100)/\left[\frac{100\ \%Fe_{end}}{\%Fe_{end} + \%Mn_{end}}\right] - M_{Mn}^{start} - M_{Fe}^{start} \quad (10)$$

M_{Fe} = mass iron melted into the alloy bath
M_{Mn} = mass manganese melted into the alloy bath
M_0 = initial carburised alloy bath mass (see Table 9)
M_{Mn}^{start}= initial manganese mass in alloy bath
M_{Fe}^{start} = initial iron mass in alloy bath
M_{Mn}^{end} = manganese mass in alloy bath at end of experiment
M_{Fe}^{end} = iron mass in alloy bath at end of experiment
$\%Mn_{start}$ = mass% Mn in alloy bath at the start of the reaction time
$\%Mn_{end}$ = mass% Mn in alloy bath at the end of the reaction time
$\%Fe_{start}$ = mass% Fe in alloy bath at the start of the reaction time
$\%Fe_{end}$ = mass% Fe in alloy bath at the end of the reaction time

Comparative total alloy production values calculated from product gas analyses and the mass balances are illustrated in Figure 17, in agreement with the trends in Figure 12: increased alloy production and alloy production rates with an increase in alloy bath temperature.

8. Conclusions

- Manganese ore smelting mechanisms reported in literature are similarly present in the AlloyStream process. Reduction of MnO solid solution and MnO dissolved in the slag are reduced by different carbon sources: carbon dissolved in alloy droplets in the reduced ore particle, solid reductant carbon at the edge of the reduced ore particle and CO gas generated in the Boudouard reaction.

- Compared to the SAF and BF processes, the relative importance of individual reactions seems to be different in the AlloyStream process. This is due to the use of smaller particle sized feed materials used and the layered structure of the furnace processing zones.

- Manganese ore smelting process control and experimental research on this subject are complicated by the interdependent factors of ore melting behaviour, ore reduction behaviour and the furnace heat input method used.

- In induction furnace smelting the alloy bath temperature, and thus heat transfer rate, has a strong effect on production rate. An increase in alloy bath temperature of ±150°C resulted in doubling of the maximum instantaneous production rate.

- In the induction furnace smelting experiments the alloy bath chemistry had little effect on instantaneous production rate. Negligible reduction of MnO by carbon dissolved in the alloy bath occurred.

- The AlloyStream process provides some benefits compared with current industrial processes (the SAF and BF), such as the ability to process fine materials (-10 mm) directly without any agglomeration; use of large proportions of carbonate ore without prior sintering since furnace eruptions is negated; most of the process energy is supplied in situ from coal and fuel gas combustion instead of outside electricity supply.

Acknowledgements

The author thanks Exxaro Resources for permission to publish this paper.

9. References

Ahmed, A., Halfa, H., El-Fawakhry, M.K., El-Faramawy, H., Eissa, M., 2014. Parameters affecting energy consumption for producing high carbon ferromanganese in a closed submerged arc furnace. *Journal of Iron and Steel Research, International*, vol. 21, pp. 666-672.

Akdogan, G., Eric, R.H., 1995. Kinetics of the solid-state carbothermic reduction of Wessel manganese ores. *Metall. Mater. Trans.* B, vol. 26B, pp. 13-24.

ASTM A99-03(2014), Standard Specification for Ferromanganese, ASTM International, West Conshohocken, PA, 2014, www.astm.org

Bale, C.W., Chartrand, P., Degterov, S.A., Eriksson, G., 2002. FactSage thermochemical software and databases. *CALPHAD*, 26, 189-228.

Barcza, N.A., Barker, I.J., Rennie, M.S., Brereton-Stiles, P.J., 2002. The application and scale-up of a.c. and d.c. smelting furnaces for ferro-alloys. *60th Electric Furnace Conference Proceedings*, vol. 60, Warrendale, PA: Iron and Steel Society, pp. 425-437.

Barcza, N.A., Koursaris, A., See, J.B., Gericke, W.A., 1979. The 'dig out' of a 75 MVA high-carbon ferromanganese electric smelting furnace. *37th Electric Furnace Proceedings*, Warrendale, The Iron and Steel Society, AIME, Detroit, USA, pp. 19-33.

Braga, R.S., Takano, C., Mourao, M.B., 2007. Prereduction of self-reducing pellets of manganese ore. *Ironmaking and Steelmaking*, vol.34, pp.279-284.

Chetty, D., Gutzmer, 2018. Quantitative mineralogy to address energy consumption in smelting of ores from the Kalahari Manganese Field, South Africa. *INFACON XV, The Fifteenth International Ferroalloys Congress*, Cape Town, South Africa, 25-28 February.

Coetsee, T., 2019. The role of manganese ore reduction morphology development in setting reduction mechanisms. *Minerals Engineering*, vol. 137, pp. 217-231.

Coetsee, T., 2018. MnO reduction in high carbon ferromanganese production: practice and theory. *Mineral Processing and Extractive Metallurgy Review*, vol.39, pp. 351-358.

Coetsee, T., 2017. The effect of processing parameters on ferromanganese alloy carbon content in Mamatwan ore reduction. *Mineral Processing and Extractive Metallurgy Review*, vol.38, pp. 116-125.

Coetsee, T., Nell, J., Pistorius, P.C., 2017. Phase characterization of high basicity manganese slags. *Metall. Mater. Trans. B*, vol. 48B, pp. 1463-1485.

Coetsee, T., Muller, J., Groenewald, J.A., du Toit, A.A., Zeelie, D., 2015a. The AlloyStream process for HCFeMn production. *INFACON XIV*, *The Fourteenth International Ferroalloys Congress*, Kiev, Ukraine, 31 May –4 June 2015, pp. 91-98.

Coetsee, T., Reinke, C., Nell, J., Pistorius, P.C., 2015b. Reduction mechanisms in manganese ore reduction. *Metall. Mater. Trans.* B, vol. 46B, pp. 2534-2552.

Crawford, D.P., Mayfield, P.L.J., Brent, A.D., Olsen, A.H., 1995. Direct production of ferromanganese from GEMCo sand concentrate and coal. *INFACON VII*, *The Seventh International Ferroalloys Congress*,Trondheim, Norway, June 1995, pp. 239-248.

Cusack, B.L., Wingrove, G.S., Hardie, G.J., 1995. Initial operation of the Hismelt® research and development facility. *Iron and Steelmaker*, February, pp. 13-20.

De Oliveira, J. R., Assis, P.S., da Silva, C.A., Alberto, J.,Tenorio, S., 1999. Kinetics study of the reduction of MnO slags and carbon dissolution in Fe-Mn baths. *EPD Congress 1999 (TMS Annual Meeting)*, San Diego, USA, 28 February-4 March 1999, pp. 259-267.

Eric, R.H., Burucu, E., 1992. The mechanism and kinetics of the carbothermic reduction of Mamatwan manganese ore fines. *Minerals Engineering*, vol. 5, pp. 795-815.

Fourie, L.J., 2000. Metal containing compound reduction and melting process. US patent 6146437.

Gaal, S., Berg, K., Tranell, G., Olsen, S., Tangstad, M., 2004. An investigation into aspects of liquid phase reduction of manganese and silica containing slag. *Proceedings of the 7th International Conference on Molten Slags, Fluxes and Salts*, Cape Town, South Africa, pp. 651-657.

Gaal, S., Lou, D., Wasbo, S., Ravary, B., Tangstad, M., 2007. Melting phenomena in ferrromanganese production. *INFACON XI*, *The Eleventh International Ferroalloys Congress*, New Delhi, India, 18-21 February, pp. 247-257.

Gasik, M. (ed.) Handbook of Ferroalloys, Elsevier Ltd., 2013.

Gericke, W.A., 1989. A techno-economic assessment of large and small furnaces. *INFACON III*, *The Third International Ferroalloys Congress*, Tokyo, Japan, 8-11 May 1983, pp. 91-102.

Gericke, W.A., 1989. The establishment of a 500 000 t/a sinter plant at Samancor's Mamatwan ore mine. *INFACON V*, *The Fifth International Ferroalloys Congress*, New Orleans, USA, 23-26 March 1989, pp. 24-33.

Gordon, Y., Nell, J., 2013. Methods of manganese ore thermal-treatment prior to smelting-what to choose? *INFACON XIII*, *The Thirteenth International Ferroalloys Congress*, Almaty, Kazakhstan, 9–13 June 2013, pp. 5-16.

Hofmann, W., Vlajcic, T., Rath, G., 1989. The rotary hearth furnace direct reduction process-a coal-based route to substitute electrical energy in ferro-alloy production. *INFACON V*, *The Fifth International Ferroalloys Congress*, New Orleans, USA, 23-26 March 1989, pp. 185-195.

International Manganese Institute (IMnI), IMnI 2018 Annual Statistics Booklet. www.manganese.org

Jang, D., Kim, Y., Shin, M., Lee, J., 2012. Kinetics of carbon dissolution of coke in molten iron. *Metall. Mater. Trans. B*, vol. 43B, pp. 1308-1314.

Jones, R.T., Barcza, N.A., Curr, T.R., 1993. Plasma developments in Africa. *Second International Symposium: World progress in plasma applications*. Palo Alto, California, 9-11 February 1993, pp. 1-18.

Kamalpour, S., Rankin, W.J., 2004. The Behaviour of coke in submerged arc furnace smelting of ferromanganese. *INFACON X*, *The Tenth International Ferroalloys Congress*, Cape Town, South Africa, 1–4 February 2004, pp. 381-391.

Kamei, Y., Miyazaki, T., Yamaoka, H., 1993. Production test of high-carbon ferromanganese using a shaft furnace with coke packed bed injected with high oxygen enriched air and a large quantity of pulverized coal. *ISIJ International*, vol.335, pp. 259-266.

Kleyenstüber, A.S.E., 1984. The mineralogy of the Manganese-bearing Hotazel formation, of the Proterozoic Transvaal sequence in Griqualand West, South Africa. Transactions of the Geological Society of South Africa, vol. 87, pp. 257-272.

Kleyenstüber, A.S.E.: M.Sc. thesis (in Afrikaans: 'n Mineralogiese ondersoek van hoë-temperatuur-reduksieprodukte van mangaanerts vanuit die Mamatwan, Kalaharimangaanveld), Rand Afrikaans University, Johannesburg, South Africa, 1979.

Koursaris, A., Kleyenstüber, A.S.E., Finn, C.W.P., 1983. A mineralogical investigation of the reduction of Mamatwan manganese ore with carbon. *Special Publication, Geological Society of South Africa*, vol.7, pp.375-382.

Koursaris, A., Finn, C.W.P., 1985. The reduction of Mamatwan ore in a submerged-arc furnace. *Transactions ISIJ*, vol. 25, pp. 109-117.

Koursaris, A., See, J.B., 1979. Reactions in the production of high-carbon ferromanganese from Mamatwan ore. *J S. Afr. Inst. Min. Metall.*, 79, pp. 149-158.

Kozhemyachenko, Y.N., Pervushin, S.I., Varava, V.I., Strelets, A.I., Vasyura, G.G., Osadchii, V.P., Nikolaev, Y.V., Anishchenko, Y.V., Shubravyi, N.S., 1987. Efficient blast regime in the production of blast-furnace ferromanganese. *Metallurgist*, vol. 31, pp. 354-358.

Lee, J., Hoai, L.T., Shin, M., 2011. Density and surface tention of liquid Fe-Mn alloys. *Metall. Mater. Trans.* B, vol. 42B, pp. 546-549.

Lee, Y.E., Tangstad, M., 2010. Electric paramters for an efficient smelting performance of HCFeMn alloy. *INFACON XII*, *The Twelfth International Ferroalloys Congress*, Helsinki, Finland, 6-9 June 2010, pp. 569-578, 2010.

Liu, B., Zhang, Y., Lu, M., Su, Z., Li, G., Jiang, T., 2019. Extraction and separation of manganese and iron from ferruginous manganese ores: A review. *Minerals Engineering*, vol. 131, pp. 286-303.

Lourens, L.L., 2008. M.Eng thesis: Reduction of iron ore fines in the Ifcon furnace. University of Pretoria, Pretoria, South Africa.

Masukawa, M., Shiota, T., 2007. *INFACON XI*, *The Eleventh International Ferroalloys Congress*, New Delhi, India, 18-21 February 2007, pp. 195-205.

Miyauchi, Y., Mochida, M., Fuchi, Y., 2001. High thermal electrical property of manganese ore production of high carbon ferromanganese, *INFACON IX*, *The Ninth International Ferroalloys Congress*, Quebec City, Canada, 3-6 June 2001, pp. 236-243.

Olsen, S.E., Tangstad, M., Lindstad, T. Production of Manganese Ferroalloys, Tapir Academic Press, Trodheim, 2007.

Olsen, S.E., Tangstad, M., 2004. The behaviour of coke in submerged arc furnace smelting of ferromanganese. *INFACON X*, *The Tenth International Ferroalloys Congress*, Cape Town, South Africa, 1–4 February 2004, pp. 231-238.

Olso, V., Tangstad, M., Olsen, S.E., 1998. Reduction kinetics of MnO-saturated slags. *INFACON VIII*, *The Eigth International Ferroalloys Congress*, Beijing, China, 7-10 June 1998, pp. 279-283.

Ostrovski, O., Olsen, S.E., Tangstad, M., Yastreboff, M., 2001. Kinetic modelling of MnO reduction from manganese ore. *INFACON IX*, *The Ninth International Ferroalloys Congress*, Quebec City, Canada, 3-6 June 2001, pp. 302-312.

Ostrovski, O., Olsen, S.E., Tangstad, M., Yastreboff, M., 2002. Kinetic modelling of MnO reduction from manganese ore. *Canadian Metallurgical Quarterly*, vol. 41, pp. 309-318.

Ostrovski, O., Swinbourne, D., 2013. Slags in production of manganese alloys. *Steel Research International*, vol. 84, pp. 680-686.

Ostrovski, O. I., Webb, T.J.M., 1995. Reduction of siliceous manganese ore by graphite. *ISIJ International*, vol. 35, pp. 1331-1339.

Pais, J., Brown, W., Saab, M. W., 1998. Production of HCFeMn using high proportions of sinter in the charge. *INFACON VIII*, *The Eigth International Ferroalloys Congress*, Beijing, China, 7-10 June 1998, pp. 237-242.

Pochart, G., Joncourt, L., Touchard, N., Perdon, C., 2007. Metallurgical benefit of reactive high grade ore in manganese alloys manufacturing. *INFACON XI*, *The Eleventh International Ferroalloys Congress*, New Delhi, India, 18-21 February 2007, pp. 217-230.

Potgieter, F.J., 1980. Hoperation of an 81 MVA high carbon ferro-manganese furnace at SAMANCOR's Meyertonworks., *INFACON II*, *TheSecond International Ferroalloys Congress*, Lausanne, Switzerland, 12-16 October 1980, pp. 244-262.

Rankin, W.J., Van Deventer, J.S.J., 1980. The kinetics of the reduction of manganous oxide by graphite. . *J S. Afr. Inst. Min. Metall.*, vol. 80, pp. 239-247.

Rankin, W.J., Wynnyckyj, J.R., 1997. Kinetics of reduction of MnO powder mixtures with carbon. *Metall. Mater. Trans.* B, vol. 46B, pp. 307-319.

Ringdalen, E., Tangstad, M., Brynjulfsen, T., 2015. Melting behaviour of Mn sources-effect on furnace performance. *INFACON XIV*, *The Fourteenth International Ferroalloys Congress*, Kiev, Ukraine, 31 May –4 June 2015, pp. 436-445.

Rivlin, V.G., 1984. 14: Critical review of constitution of carbon-chromium-iron and carbon-iron-manganese systems. *International Metals Reviews*, 29, pp. 299-327.

Roscoe, R., 1952. The viscosity of suspensions of rigid spheres. *British Journal of Applied Physics.* 3, pp. 267-269.

Safarian, J., Kolbeinsen, L., 2008. Kinetic of carbothermic reduction of MnO from high-carbon ferromanganese slag by graphite materials. *ISIJ International*, vol. 48, pp. 395-404.

Safarian, J., Tranell, G., Kolbeinsen, L., Tangstad, M., Gaal, S., Kaczorowski, J., 2008. Reduction kinetics of MnO from high-carbon ferromanganese slags by carbonaceous materials in Ar and CO atmospheres. *Metall. Mater. Trans. B*, vol. 39B, pp. 702-712.

Safarian, J., Kolbeinsen, L., Tangstad, M., Tranell, G., 2009. Kinetics and mechanism of the simultaneous carbothermic reduction of FeO and MnO from high-carbon ferromanganese slag. *Metall. Mater. Trans. B*, vol. 40B, pp. 922-939.

Senin, A.V., Ivanov, A.V., Zhuralev, D.L. 2018. The degree of manganese reduction from ores in blast-furnace ferromanganese smelting at JSC "Satka Iron Smelting Works". *INFACON XV*, *The Fifthteenth International Ferroalloys Congress*, Cape Town, South Africa, 25–28 February 2018, pp. .

Schoukens, A.F.S., Curr, T.R., 1985. The production of manganese ferro-alloys in transferred-arc plasma systems. *42nd Electric Furnace Proceedings,* Warrendale, The Iron and Steel Society, AIME, Totonto, Canada, December 1985, pp. 161-171.

Skjervheim, T., Olsen, S.E., 1995.The rate and mechanism for reduction of manganese oxide from silicate slags. *INFACON VII*, *The Seventh International Ferroalloys Congress*,Trondheim, Norway, June 1995, pp. 631-639.

Sun, H., Lone, M.Y., Ganguly, S., Ostrovski, O., 2010. Wetability and reduction of MnO in slag by carbonaceous materials. *ISIJ International*, vol. 50, pp. 639-646.

Takahashi, K., Nouchi, T., Sato, M., Ariyama, T., 2015. Perspective on progressive development of oxygen blast furnace for energy saving. *ISIJ International*, vol. 55, pp. 1866-1875.

Tangstad, M., Olsen, S.E., 1997. Phase relations in ferromanganese slags during melting and reduction. *Proceedings of the 5th International Conference on Molten Slags, Fluxes and Salts*, Sydney, Australia, pp. 549-555.

Tangstad, M., Ichihara, K., Ringdalen, E., 2015. Pretreatment unit in ferromanganese production. *INFACON XIV*, *The Fourteenth International Ferroalloys Congress*, Kiev, Ukraine, 31 May –4 June 2015, pp. 99-106.

Thornton, P.A., Colangelo, V. J, 1985. Fundamentals of Engineering Materials. Prentice-Hall, Inc., Engelwood Cliffs, New Jersey, p. 399.

Urquhart, R.C., 1980. The physico-chemical properties of slags associated with the production of high-carbon ferromanganese. *Canadian Metallurgical Quarterly,* vol. 19, pp. 323-327.

U.S. Geological Survey, 2019, Mineral commodity summaries 2019: U.S. Geological Survey, https://doi.org/10.3133/70202434

Van Deventer, J.S.J., 1987. The effect of gangue components on the reduction of manganosite by graphite: An isothermal kinetic study.*Thermochimica Acta*, Vol. 112, pp. 365-377.

Visser, M., Smith, H., Ringdalen, E., Tangstad, M., 2013. Properties of Nchwaning and Gloria ore in the production of Mn ferro-alloys. *INFACON XIII*, *The Thirteenth International Ferroalloys Congress*, Almaty, Kazakhstan, 9–13 June 2013, pp. 553-565.

Wellbeloved, D.B., Craven, P.M., Waudby, J.W., 1990. Manganese and Manganese Alloys. In: Elvers, B., Hawkins, S., Schulz, G. (Eds.) *Ullmann's Encyclopedia of Industrial Chemistry.* 5th Edition. Vol. A16, pp. 77-121.

Wellbeloved, D.B., Kemink, M., 1995. The eceonomic and technical implications of the use of coal rather than coke as a reductant at Metalloys. *INFACON VII*, *TheSeventh International Ferroalloys Congress*, Trondheim, Norway, 11–14 June 1995, pp. 191-199.

Woollacott, L.C., Howat, D.D., Jochens, P.R., 1974. *INFACON I*, *The First International Ferroalloys Congress*, Johannesburg, South Africa, 22-26 April 1974, pp. 227-232.

Wu, C., Sahajwalla, V., 2000. Dissolution rates of coals and graphite in Fe-C-S melts in direct ironmaking: influence of melt carbon and sulfur on carbon dissolution. *Metall. Mater. Trans. B*, vol. 31B, pp. 243-251.

Xiaoxing, X., Daolin, L., 1998. Studies on production of high carbon ferromanganese in Blast Furnace with high proportion of sinter and improvement in manganese recovery. *INFACON VIII*, *The Eigth International Ferroalloys Congress*, Beijing, China, 7-10 June 1998, pp. 226-231.

Xu, K., Jiang, G., Ding, W., Gu, L., Guo, S., Zhao, B., 1993. The kinetics of reduction of MnO in slag with carbon saturated liquid iron. ISIJ International, vol. 33, pp. 104-108.

Yastreboff, M., Ostrovski, O., Ganguly, S., 1998. Carbothermic reduction of manganese from manganese ore and ferromanganese slag. *INFACON VIII*, *The Eigth International Ferroalloys Congress*, Beijing, China, 7-10 June 1998, pp. 263-270.

Yastreboff, M., Ostrovski, O., Ganguly, S., 2003. Effect of gas composition on the carbothermic reduction of manganese oxide. *ISIJ International*, vol. 43, pp. 161-165.

Zhang, T., 1992. The two-stage production of high-carbon ferromanganese in a Blast Furnace: a method for the treatment of a lean manganese ore. *INFACON VI*, *The sixth International Ferroalloys Congress*, Johannesburg, South Africa, 8-11 March 1992, pp. 155-159.

Table 1: Alloy compositions: ASTM specification for standard ferromanganese, ASTM A99-03(2014)

Grade	%Mn	%C max	%Si max	%P max	%S max
A	78.0-82.0	7.5	1.2	0.35	0.05
B	76.0-78.0	7.5	1.2	0.35	0.05
C	74.0-76.0	7.5	1.2	0.35	0.05

Table 2: Main process features: AlloyStream vs. SAF vs. BF

	AlloyStream	SAF	BF
Ore particle size	-10mm	-75mm +6mm	-30mm +6mm
Process energy input as electricity	30%-40%	100%	0%
Carbonate ore in ore mixture	unlimited	<30%	0%
Reductant particle size	-2mm	-75mm +6mm	-30mm +6mm
Reductant quality and cost	low cost (thermal coal)	high cost (specific requirements)	high cost (high quality coke)
Carbon balance sensitivity	low	high	medium
Slag basicity constraints	medium	high	medium
Smelting zone refractory	MgO-based	Carbon-based	Carbon-based
Electricity input efficiency	75%-85%	53%-82%[1]	not applicable
Heat losses	30%-40%	20%-27%[2,3]	18%[4]
Prodution rate	medium	high	high
Furnace exit gas temperature (°C)	1600	200	369[4]

[1]Power factor for small furnace (18MW) is 0.82 vs. for large furnace (75MW) is 0.53 (Gericke, 1983); [2]Olsen et al. (2007); [3] Ahmed et al. (2014); [4]Kozhemyachenko et al. (1987)

Table 3: de Oliveira et al. (1999): MnO reduction rate vs. Carbon dissolution rates at 1600°C

	Rate
Carbon dissolution into 5%Mn-Fe alloy	6.8×10^{-2} mol C/minute/cm^2
Carbon dissolution into 15%Mn-Fe alloy	8.3×10^{-2} mol C/minute/cm^2
MnO reduction rate: high	8.9×10^{-4} mol MnO/minute/cm^2

Table 4: MnO reduction rates from slag in g.MnO/minute/cm²

(°C)	Olso et al. (1998)	Ostrovski et al. (2001, 2002)	Safarian & Kolbeinsen (2008)	de Oliveira et al. (1999)
1400		$2.6x10^{-3}$		
1450	$1.0x10^{-3}$ to $1.9x10^{-3}$	# $8.0x10^{-3}$	$6.0x10^{-4}$	
1500	$2.1x10^{-3}$ to $4.0x10^{-3}$	# $1.6x10^{-2}$	$1.2x10^{-3}$	
1550	$4.8x10^{-3}$ to $1.5x10^{-2}$	# $3.0x10^{-2}$		
1600			$4.5x10^{-4}$	$1.3x10^{-2}$ to $6.3x10^{-2}$
Reductant:	graphite crucible	graphite particles	graphite plate	Fe-Mn-C alloy

#: extrapolated from Arrhenius equation from 1250°C-1400°C

Table 5: Carbon dissolution rate constant values, K (1/s)

Study	Graph key	°C	K (1/s)	Alloy	Carbon type
de Oliveira et al. (1999)	1_Gr(5%Mn)	1600	$3.48x10^{-2}$	5%Mn-Fe-C alloy	Graphite
de Oliveira et al. (1999)	1_Gr(15%Mn)	1600	$5.12x10^{-2}$	15%Mn-Fe-C alloy	Graphite
Wu & Sahajwalla (2000)	2_Gr(N)	1550	$1.22x10^{-2}$	Iron	Natural graphite
Wu & Sahajwalla (2000)	2_Gr(S)	1550	$2.40x10^{-2}$	Iron	Synthetic graphite
Wu & Sahajwalla (2000)	2_Coal(h)	1550	$3.61x10^{-3}$	Iron	Coal (highest)
Wu & Sahajwalla (2000)	2_Coal(l)	1550	$1.13x10^{-3}$	Iron	Coal (lowest)
Jang et al. (2012)	3_Gr	1550	$9.72x10^{-3}$	Iron	Graphite
Jang et al. (2012)	3_coke	1450	$9.41x10^{-4}$	Iron	Coke
Jang et al. (2012)	3_coke	1550	$4.33x10^{-3}$	Iron	Coke
Jang et al. (2012)	3_coke	1650	$7.73x10^{-3}$	Iron	Coke

Table 6: Pre-reduced ore and burnt dolomite bulk chemical composition (mass percentages)

	Pre-reduced ore	Burnt dolomite
MnO	78.55	1.72
FeO	9.15	1.18
SiO_2	5.57	4.77
Al_2O_3	2.85	0.31
CaO	0.33	54.68
MgO	0.15	37.13
TiO_2	0.08	0.04
K2O	0.24	0.07
BaO	2.90	0.00
P_2O_5	0.17	0.09
Total	100.0	100.0

Table 7: Eikeboom char bulk composition (mass percentages)

Proximate analysis (dry basis)	
Moisture	0.1
Volatile matter	0.4
Fixed carbon	82.7
Ash	16.9
Ultimate analysis (dry basis)	
C	79.8
H	0.35
N	1.11
O	1.48
S	0.36
Ash analysis (dry basis)	
SiO_2	54.50
Al_2O_3	36.10
Fe_2O_3	3.76
TiO_2	2.00
CaO	1.53
MgO	0.41
MnO	0.03
Na_2O	0.09
K_2O	0.56
P_2O_5	0.62
Cr_2O_3	0.23
S	0.09

Table 8: Calculated bulk slag analyses (mass percentages)

	Pre-reduced Ore (0% Mn recovery)	Feed Mixture (0% Mn recovery)	Feed Mixture (40% Mn recovery)	Feed Mixture (80% Mn recovery)
MnO	89.8	77.7	67.6	41.0
SiO_2	6.4	8.1	11.8	21.4
Al_2O_3	3.3	4.2	6.2	11.2
CaO	0.4	6.0	8.7	15.8
MgO	0.2	4.0	5.8	10.5
Total	100.0	100.0	100.0	100.0
B2	0.06	0.74	0.74	0.74
B3	0.09	1.23	1.23	1.23

Table 9: Experimental conditions

Sample Name	Alloy bath temperature (°C)	Initial alloy bath chemistry	Initial %C in alloy bath	Reduction experiment duration (minutes)	Initial alloy bath mass (g.)	Feed mixture mass fed (g.)
1	1542	Iron	2.5	96	5104	2000
2	1565	Iron	3.1	31	5136	2000
3	1385	Iron	3.0	89	5127	2000
4	1420	Ferromanganese	3.3	91	5089	2000

Table 9: Experimental conditions

Sample Name	Alloy bath temperature (°C)	Initial alloy bath chemistry	Initial %C in alloy bath	Reduction experiment duration (minutes)	Initial alloy bath mass (g.)	Feed mixture mass fed (g.)
1	1542	Iron	2.5	96	5104	2000
2	1565	Iron	3.1	31	5136	2000
3	1385	Iron	3.0	89	5127	2000
4	1420	Ferromanganese	3.3	91	5089	2000

Table 10: Manganese and carbon activities in experiment 3 and 4 alloy bath compositions

Experiment	Start or End composition	Alloy bath temperature (°C)	$a_{Mn(l)}$	$a_{C(l)}$	$a_{Mn(l)}/a_{C(l)}$	$RTln(a_{Mn(l)}/a_{C(l)})$ [J]	ΔG[J]
3	Start	1385	3.34×10^{-3}	1.12×10^{-3}	3	15022	-69347
3	Start	1420	3.45×10^{-3}	1.31×10^{-3}	3	13669	-75564
3	End	1385	1.24×10^{-2}	1.49×10^{-3}	8	29197	-55172
3	End	1420	1.29×10^{-2}	1.74×10^{-3}	7	28209	-61024
4	Start	1385	6.08×10^{-1}	5.14×10^{-4}	1184	97264	12895
4	Start	1420	6.07×10^{-1}	6.11×10^{-4}	992	97124	7891
4	End	1385	4.94×10^{-1}	1.46×10^{-3}	338	80041	-4328
4	End	1420	4.89×10^{-1}	1.73×10^{-3}	164	79575	-9657

From FactSage 6.4 reaction module: $\Delta G^{\circ}_{1385^{\circ}C}$ = -84369 J/mol; $\Delta G^{\circ}_{1420^{\circ}C}$ = -89233 J/mol

Table 11: Alloy bath starting conditions

Sample Name	Alloy bath temperature (°C)	Initial alloy bath chemistry	mass% Fe	mass% Mn	mass% C	mass% Si	Total %
1	1542	Iron	97.0	0.4	2.5	0.10	99.98
2	1565	Iron	96.1	0.6	3.1	0.14	99.94
3	1385	Iron	96.2	0.7	3.0	0.15	99.96
4	1420	Ferromanganese	17.7	78.8	3.3	0.16	99.99

*For all starting alloys: %S<0.03

Table 12: Final alloy bath composition

Sample Name	Alloy bath temperature (°C)	Initial alloy bath chemistry	%Fe	%Mn	%C	%Si	Total %
1	1542	Iron	90.0	6.0	4.0	0.01	99.99
2	1565	Iron	91.9	4.0	4.1	0.01	100.01
3	1385	Iron	93.7	2.8	3.5	0.01	100.01
4	1420	Ferromanganese	16.7	78.0	5.0	0.27	99.97

* For all end point alloys: %S<0.01

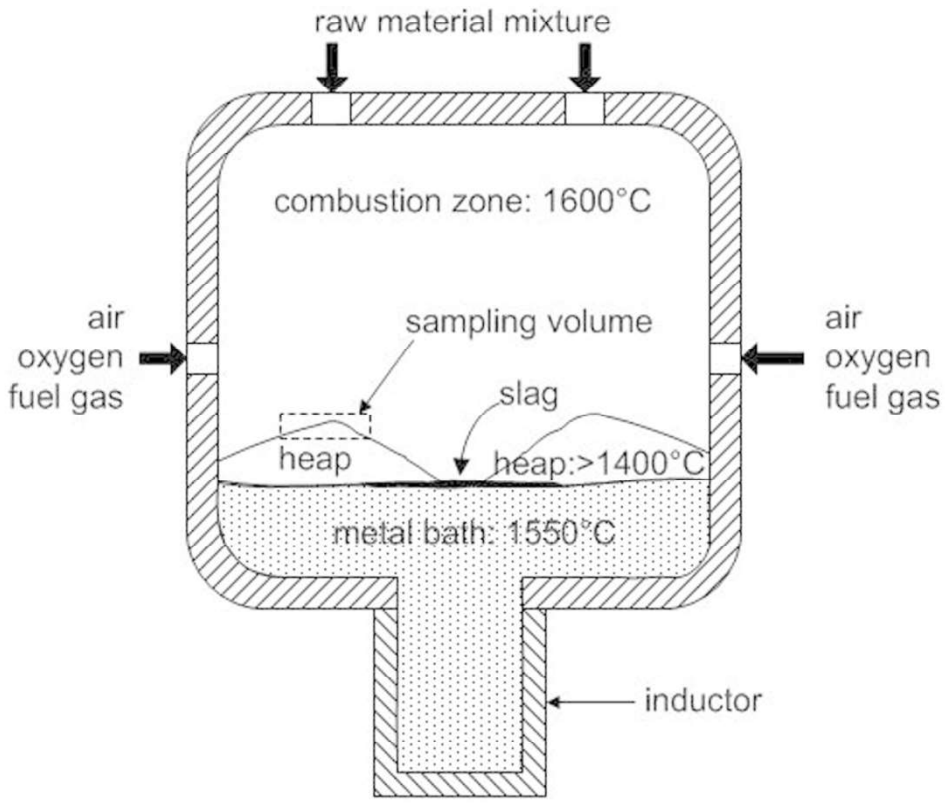

Figure 1: Furnace cross-section

80x70mm (600 x 600 DPI)

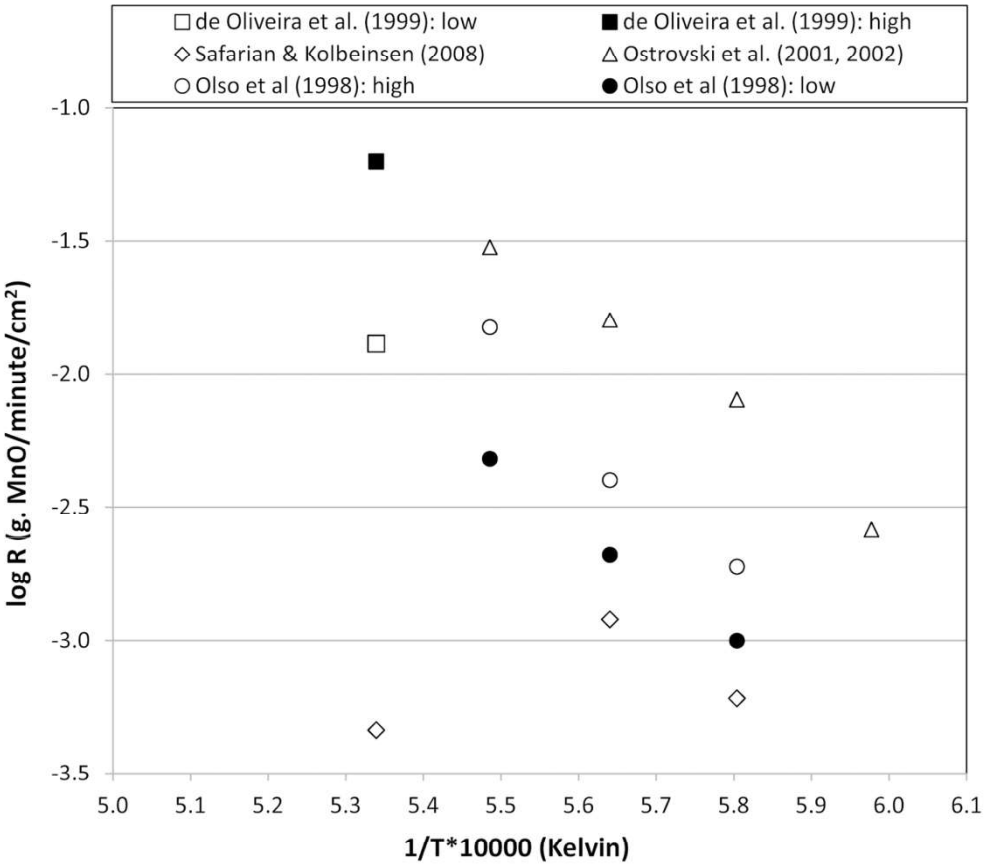

Figure 2: MnO reduction rates by graphite carbon (solid and dissolved in Fe-Mn-C alloy)

80x70mm (600 x 600 DPI)

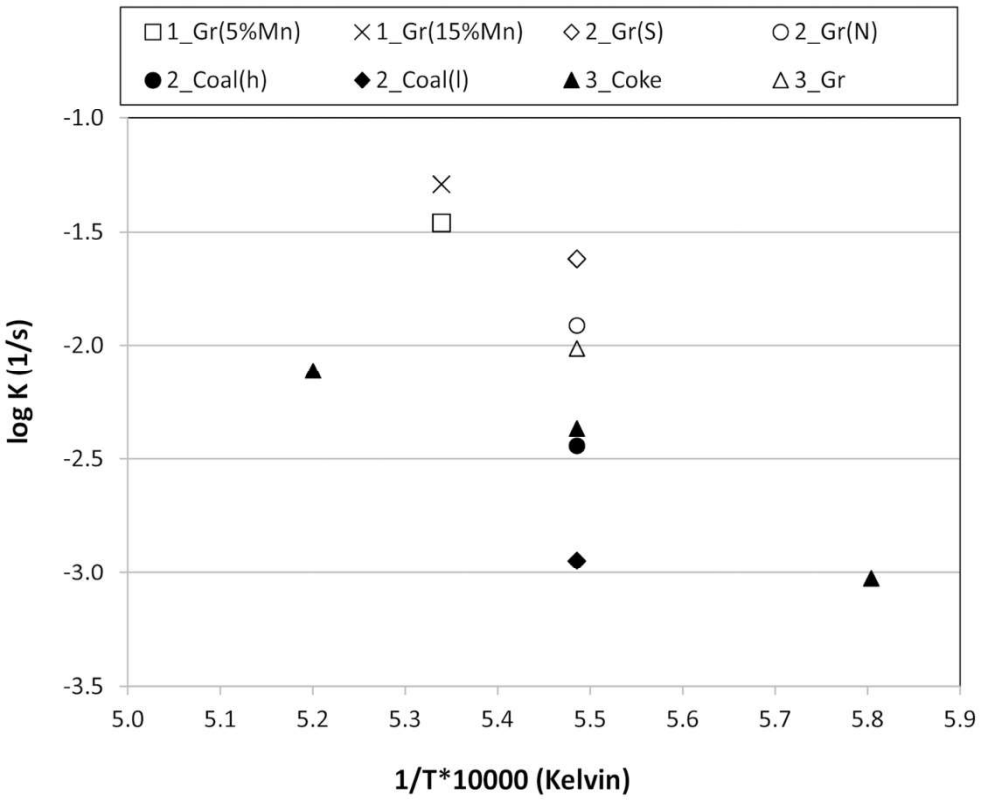

Figure 3: Carbon dissolution into iron and Fe-Mn-C alloy: rate constant values, K (1/s)

79x66mm (600 x 600 DPI)

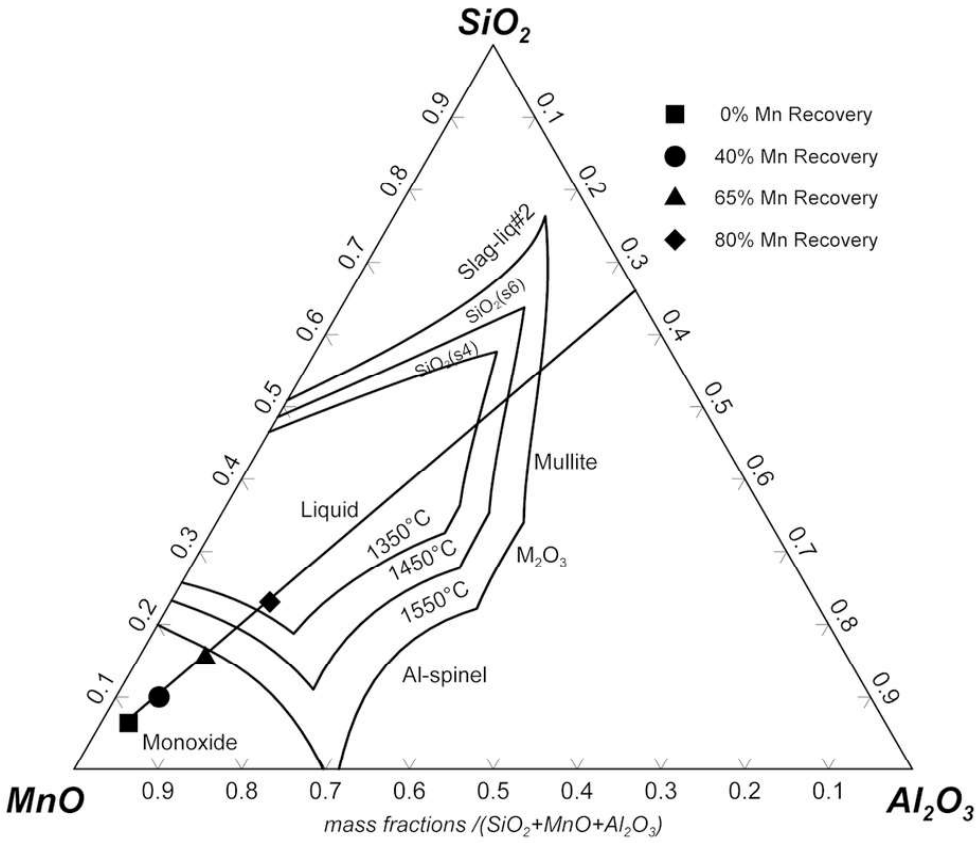

Figure 4(a): Pre-reduced ore composition at 0% manganese recovery (%MgO=0; %CaO=0)

80x68mm (300 x 300 DPI)

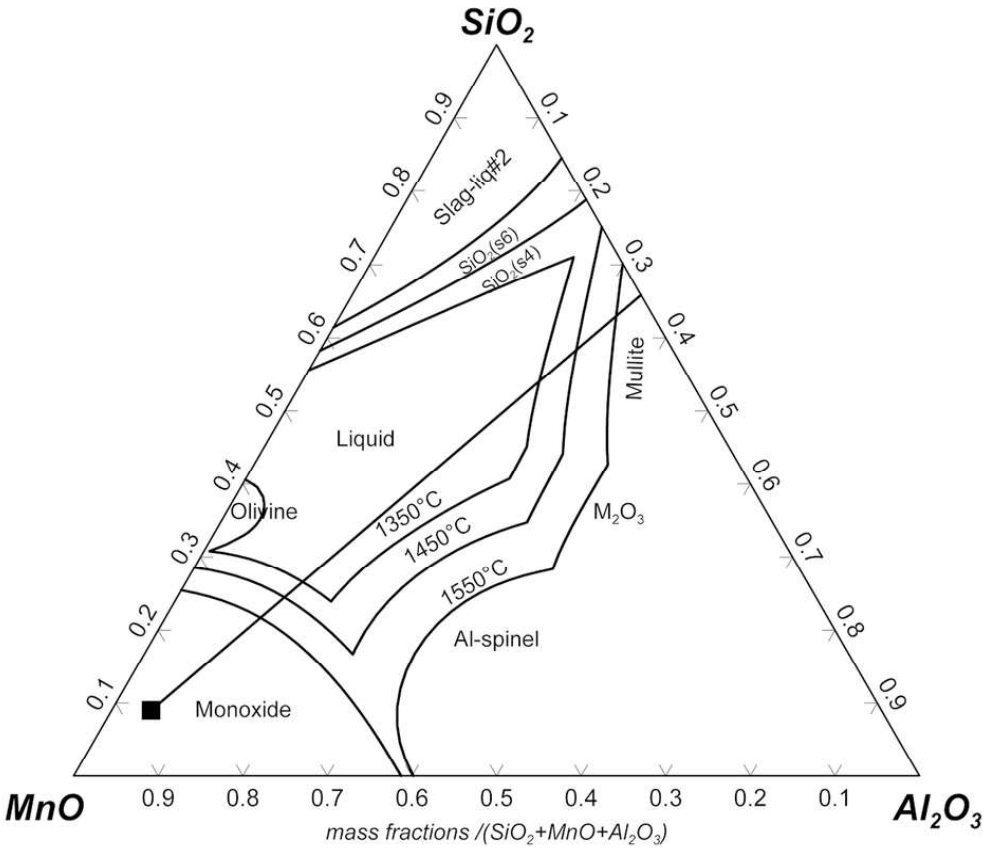

Figure 4(b): Expected bulk slag composition at 0% manganese recovery (%MgO=4; %CaO=6)

80x69mm (300 x 300 DPI)

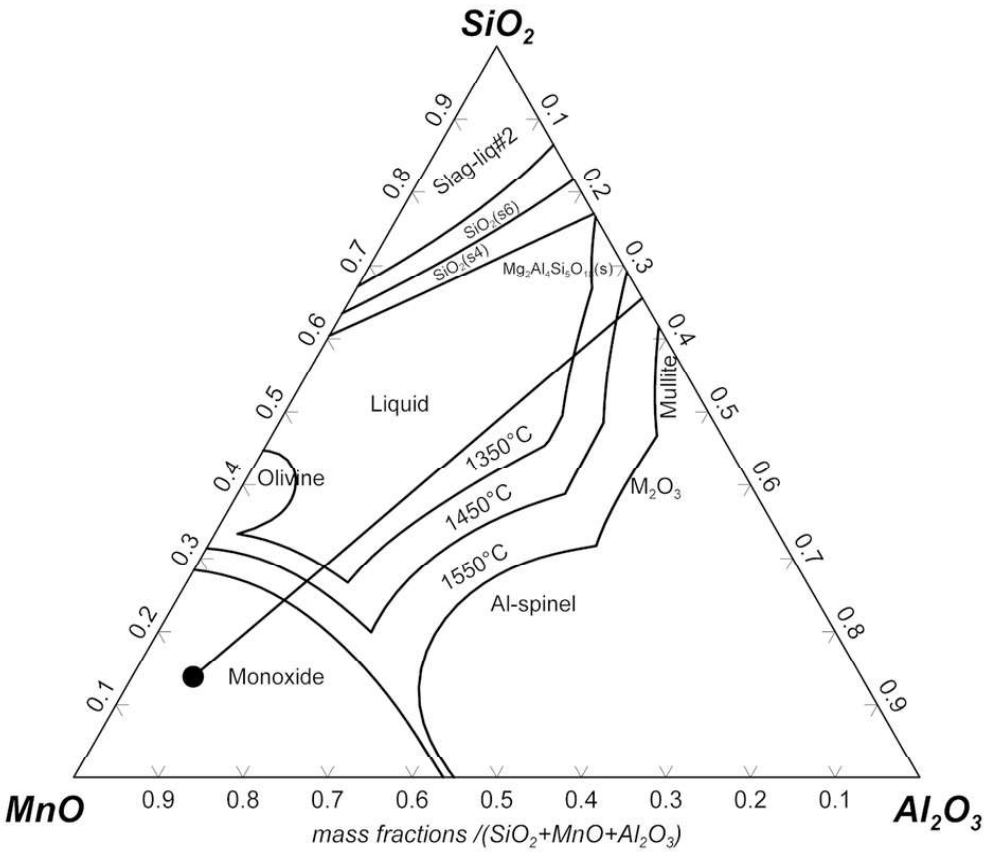

Figure 4(c): Expected bulk slag composition at 40% manganese recovery (%MgO=6; %CaO=9)

80x69mm (300 x 300 DPI)

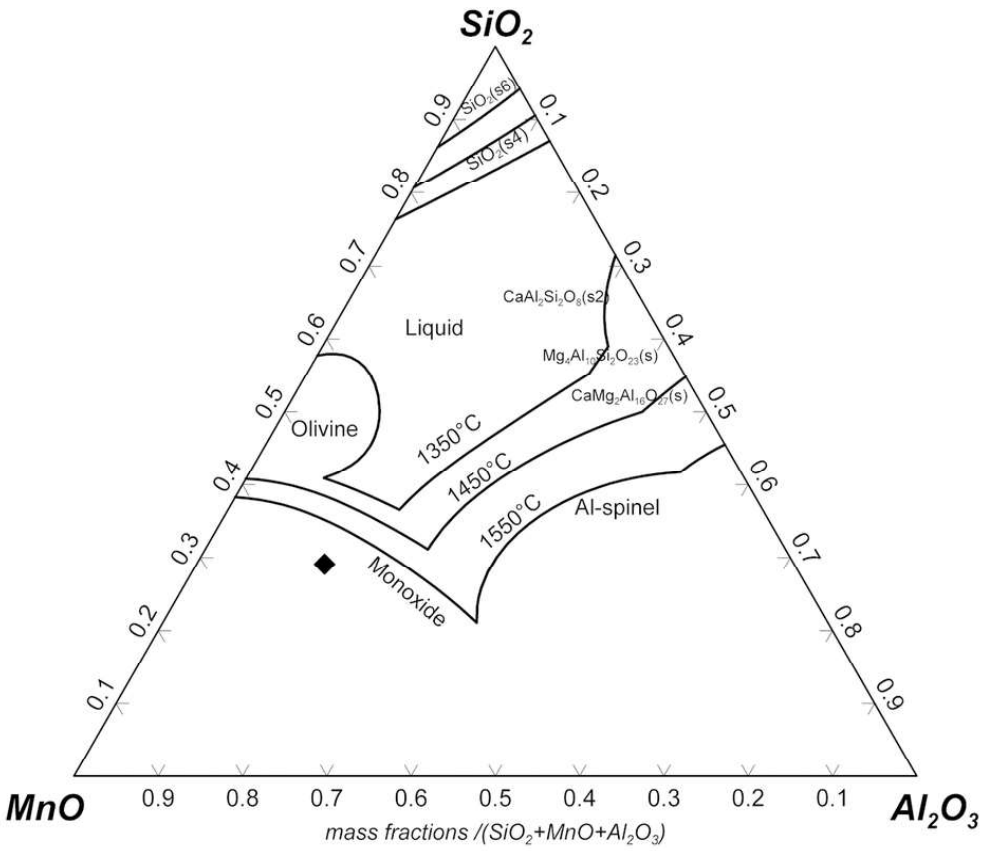

Figure 4(d): Target slag composition at 80% manganese recovery (%MgO=11; %CaO=16)

80x69mm (300 x 300 DPI)

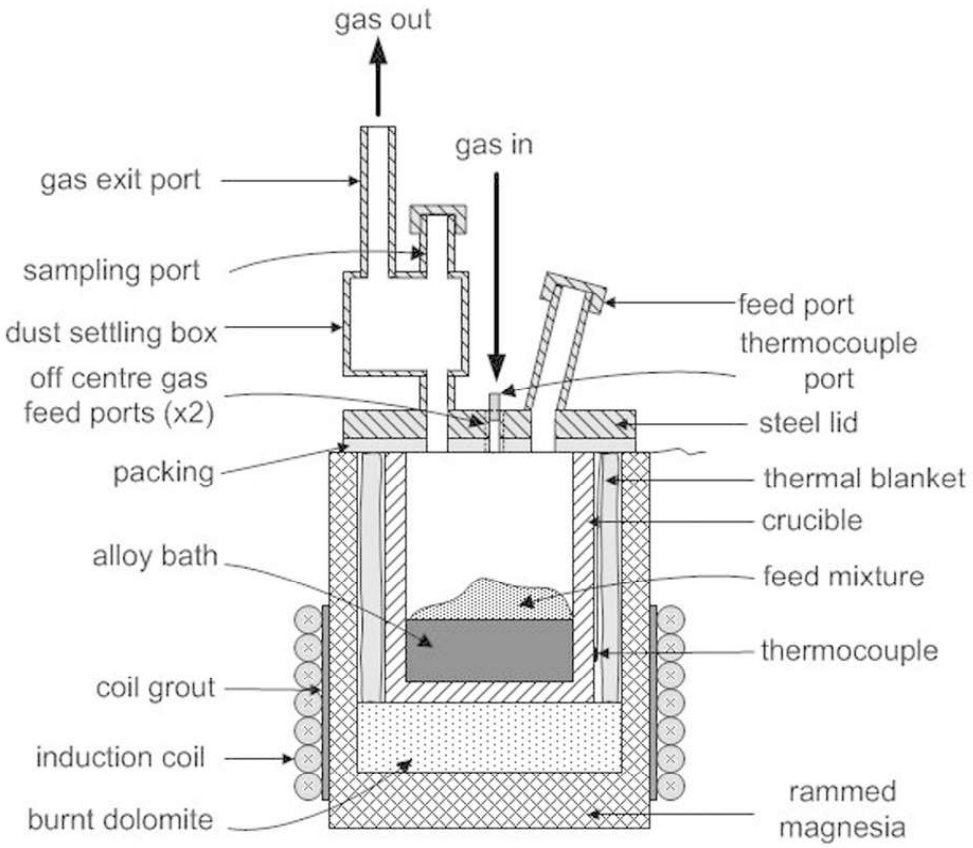

Figure 5: Experimental set-up: induction furnace

80x68mm (300 x 300 DPI)

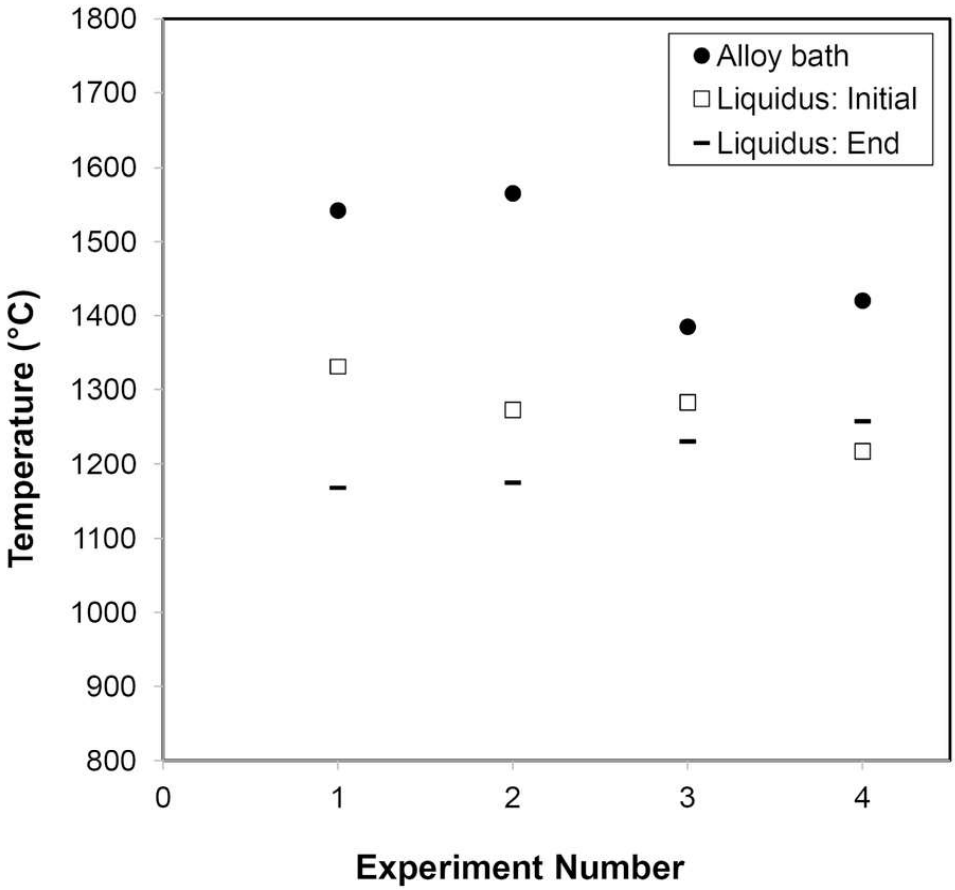

Figure 6: Alloy bath superheat levels

80x73mm (300 x 300 DPI)

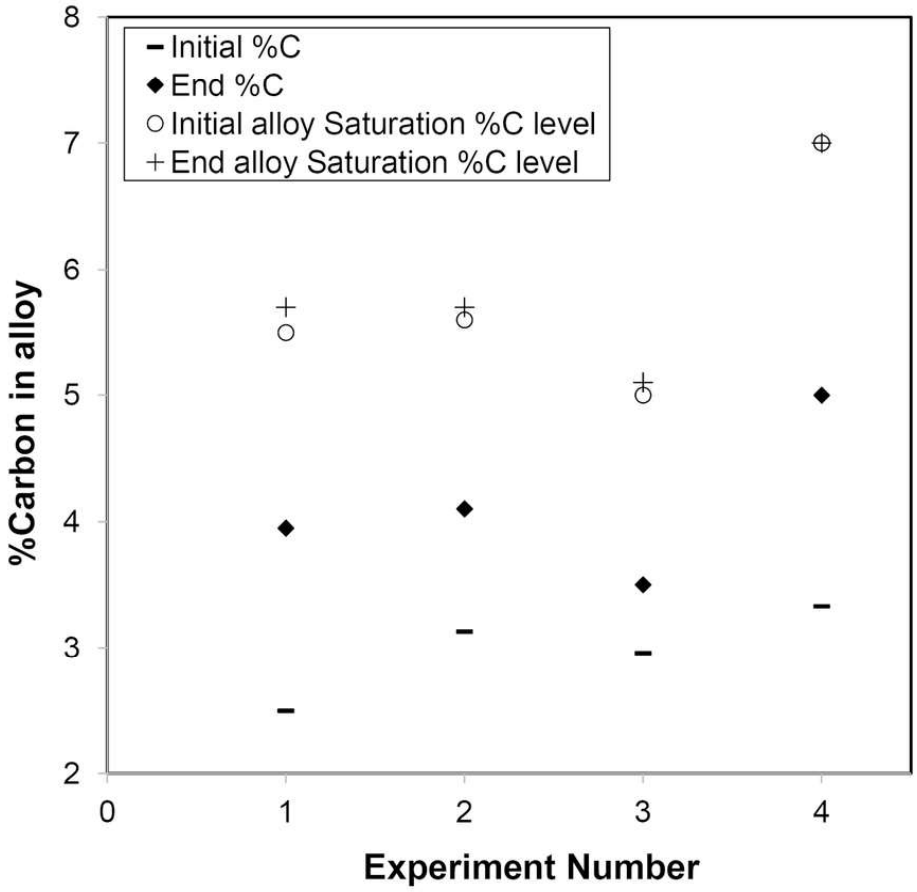

Figure 7: Alloy bath carbon content

80x74mm (300 x 300 DPI)

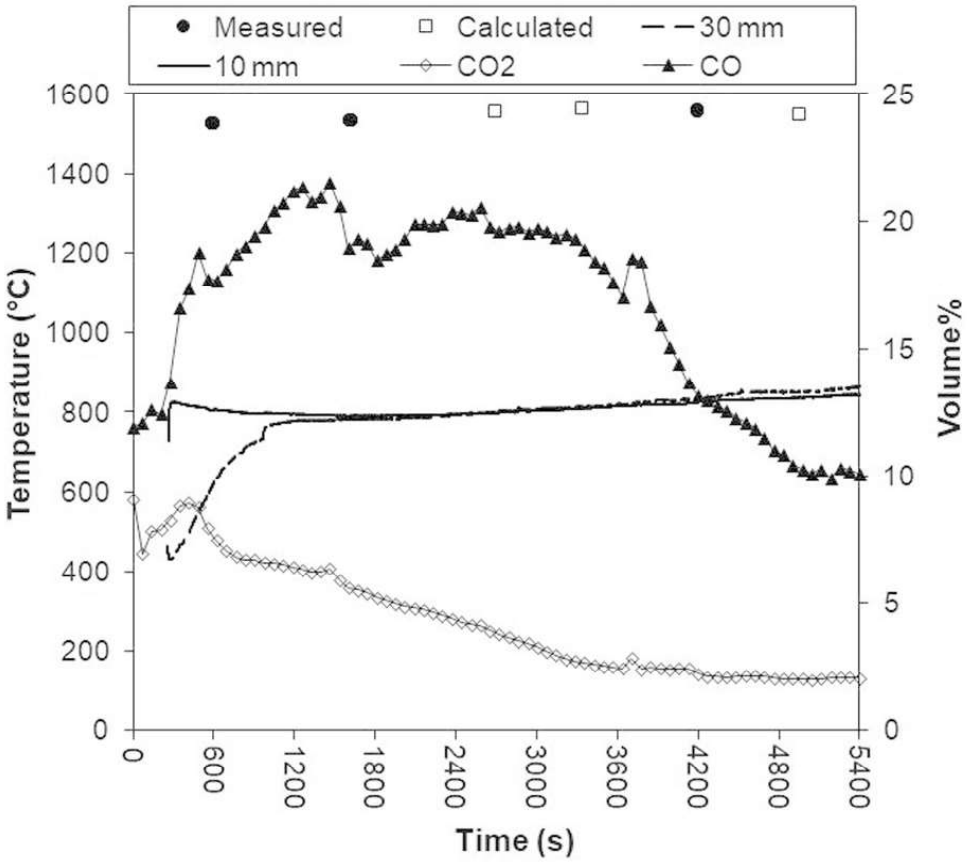

Figure 8: Measurements in Experiment 1 (Iron bath at 1542°C)

80x69mm (300 x 300 DPI)

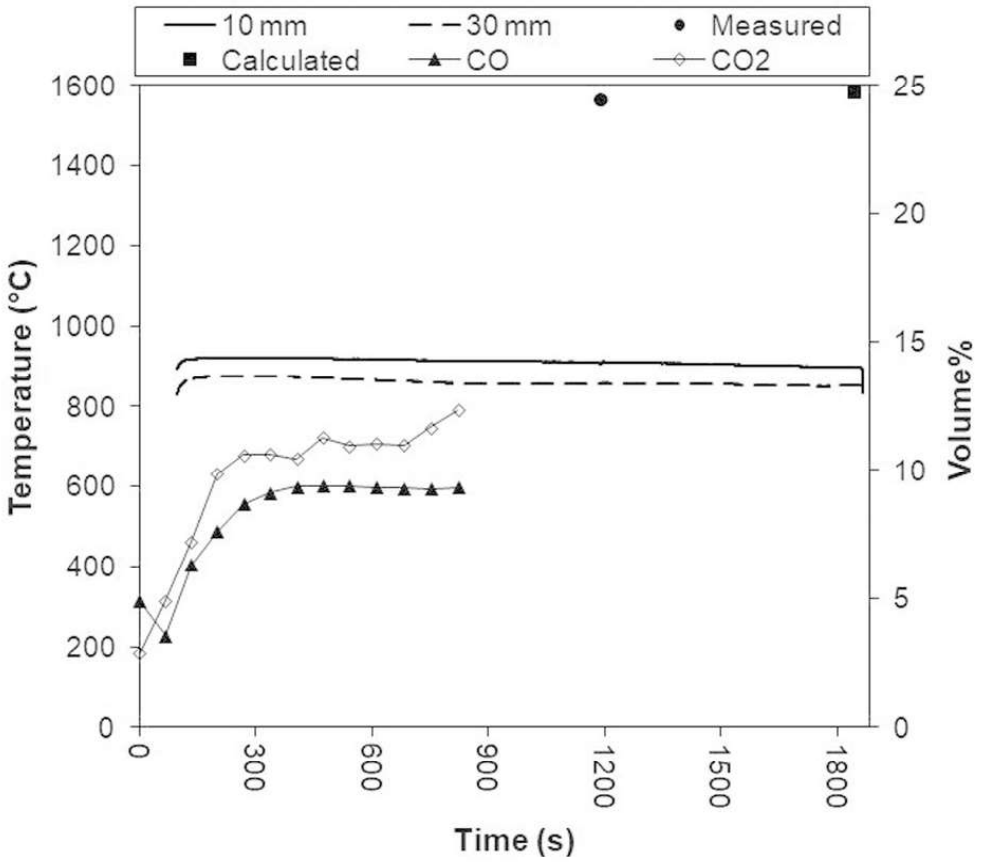

Figure 9: Measurements in Experiment 2 (Iron bath at 1565°C)

80x70mm (300 x 300 DPI)

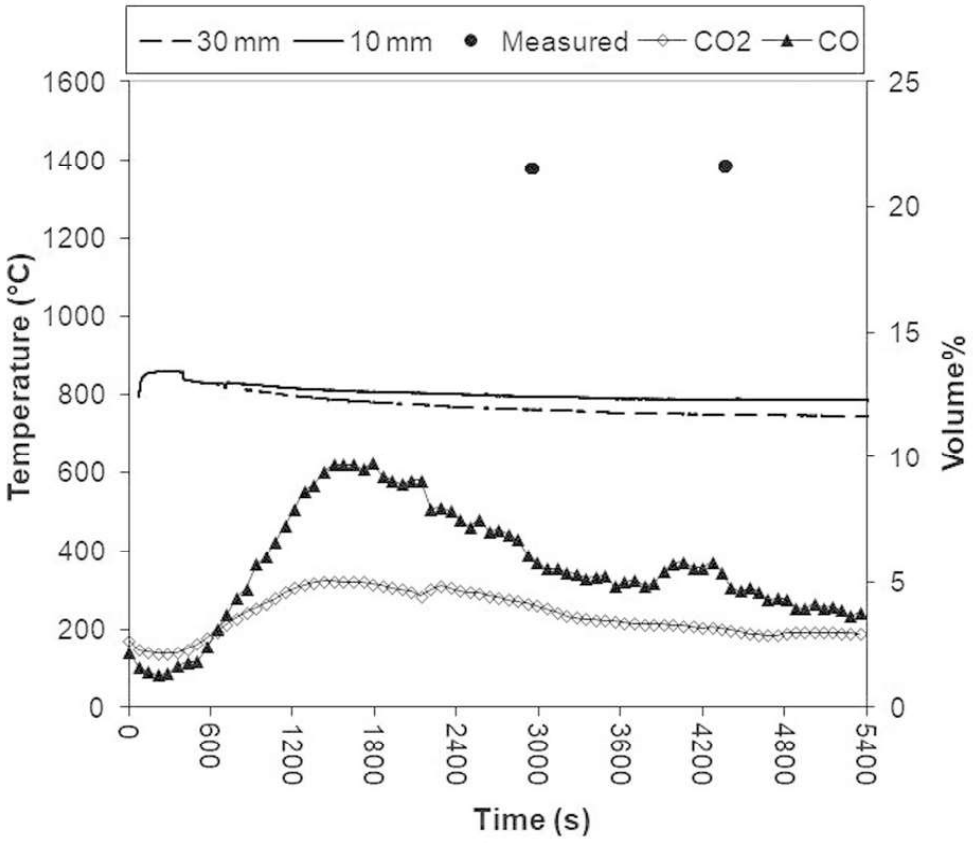

Figure 10: Measurements in Experiment 3 (Iron bath at 1385°C)

80x69mm (300 x 300 DPI)

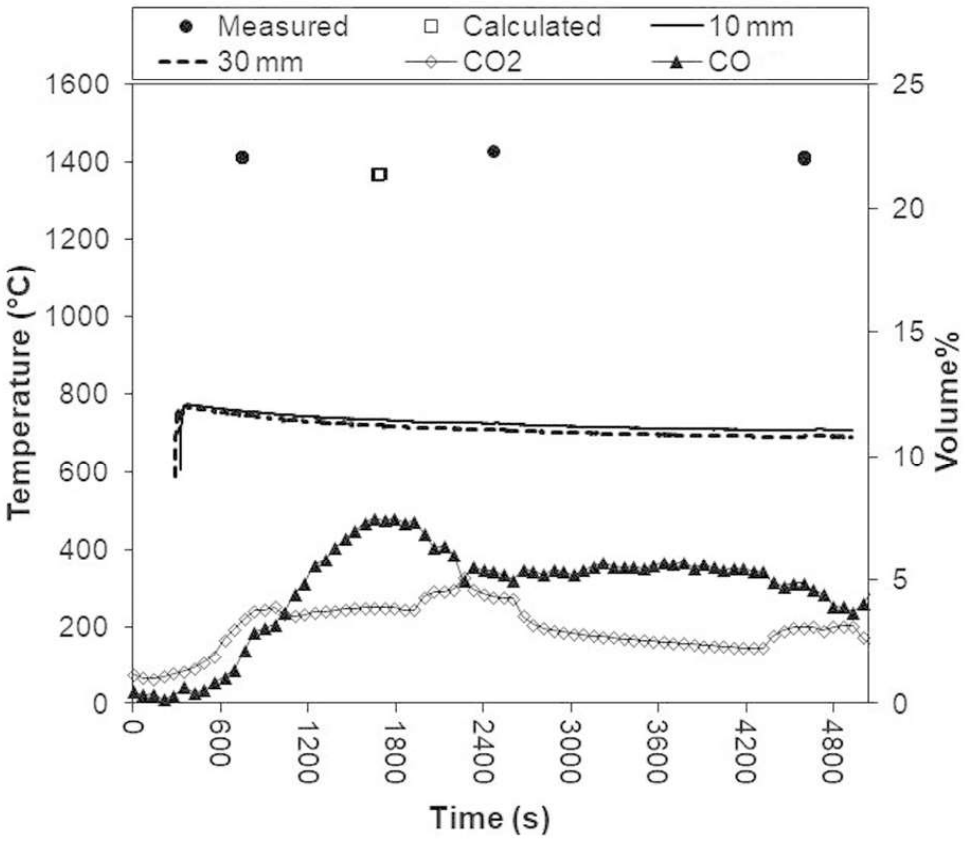

Figure 11: Measurements in Experiment 4 (Ferromanganese bath at 1420°C)

80x69mm (300 x 300 DPI)

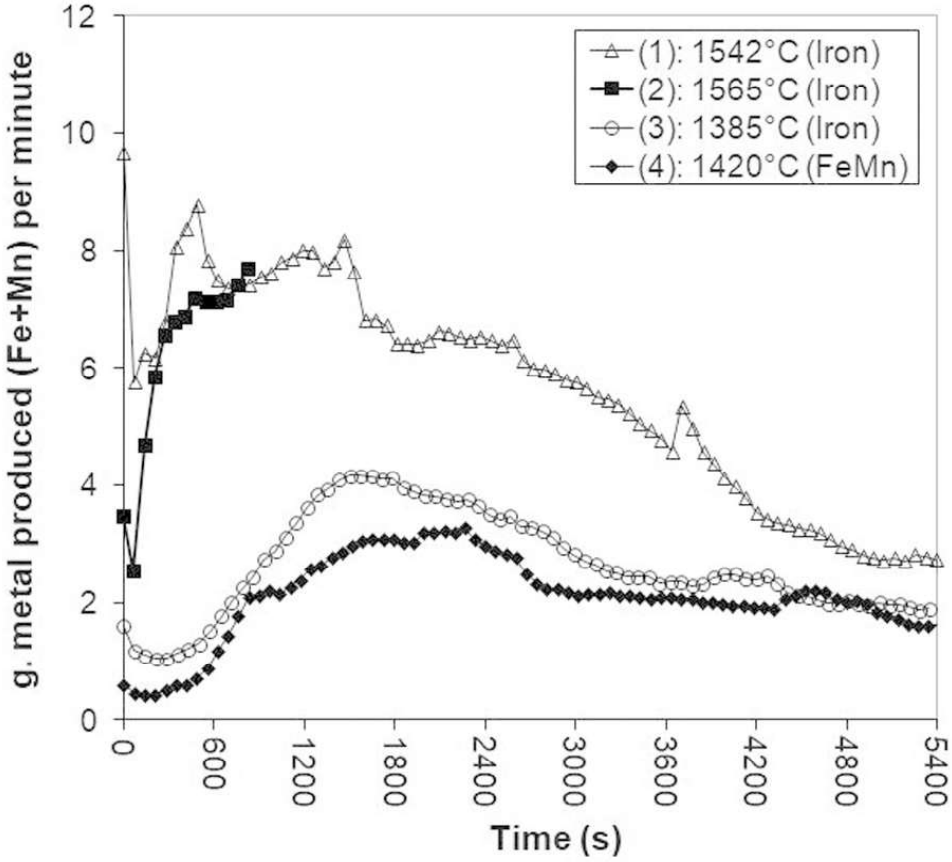

Figure 12: Relative instantaneous production rates

80x70mm (300 x 300 DPI)

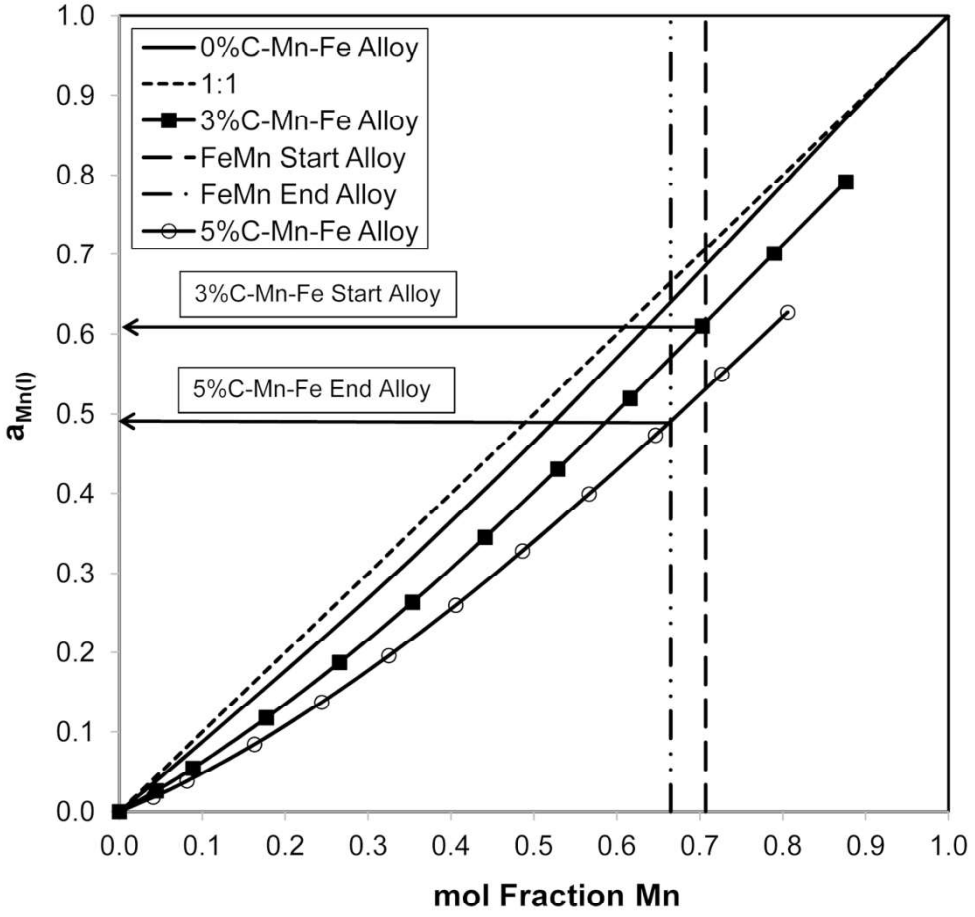

Figure 13: Manganese activity at 1500°C

80x75mm (600 x 600 DPI)

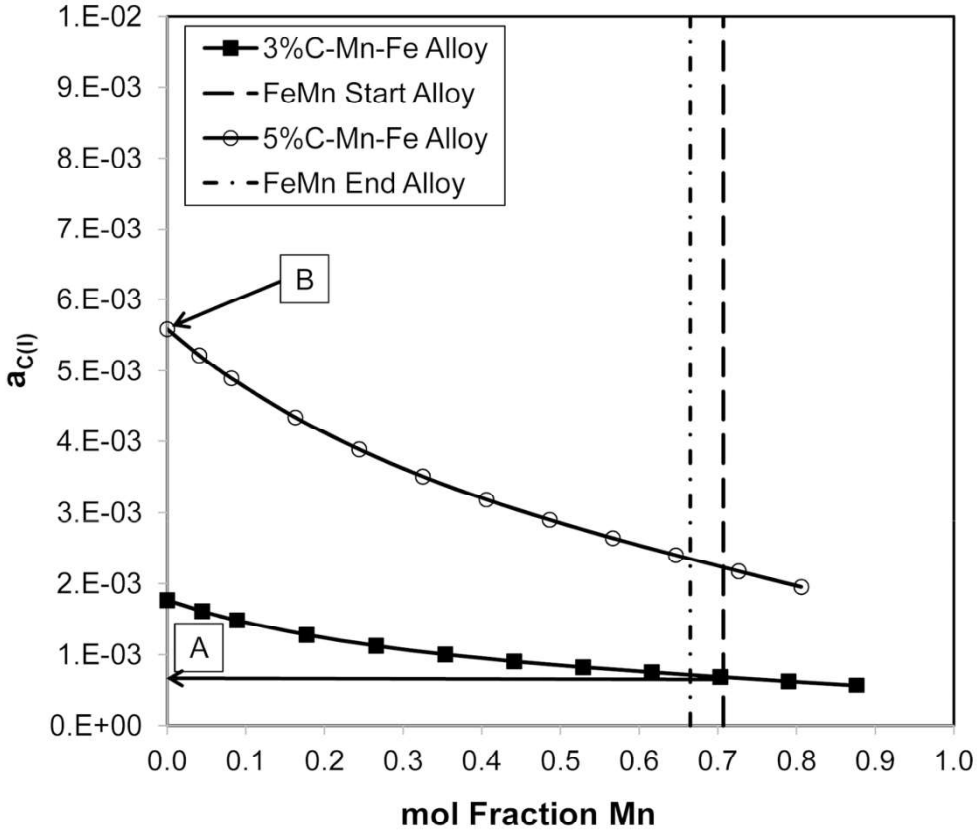

Figure 14: Carbon activity at 1500°C

79x70mm (600 x 600 DPI)

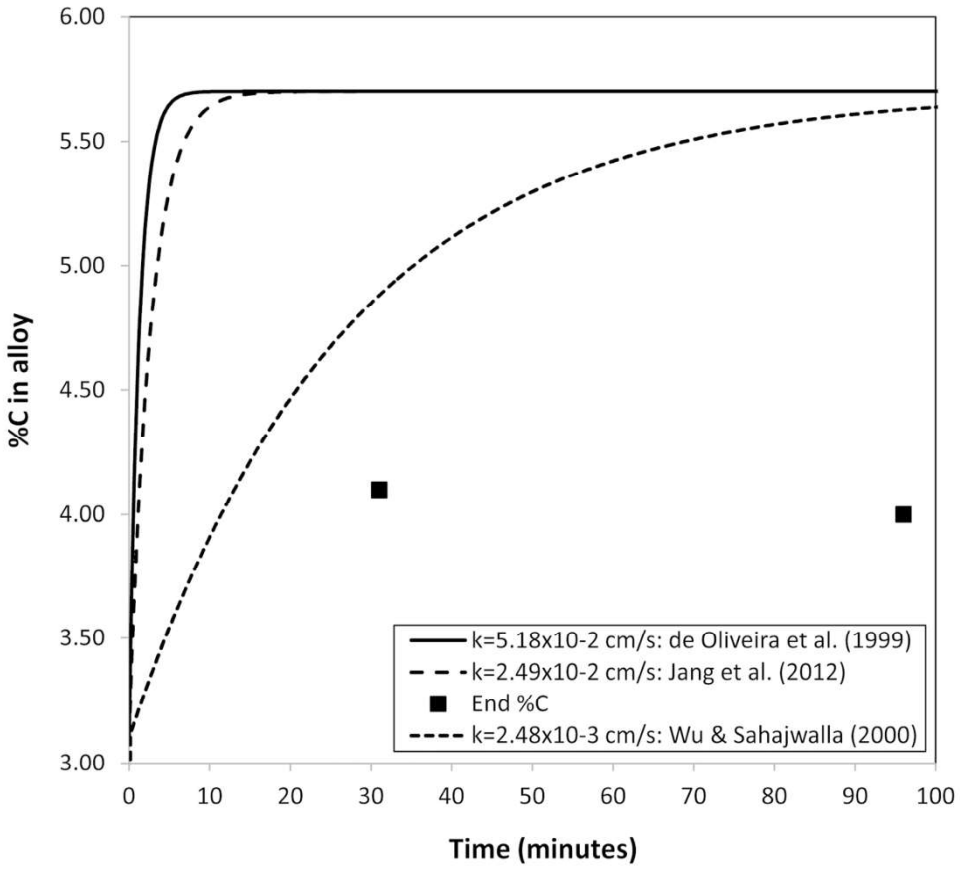

Figure 15: Carbon dissolution rate calculations vs. actual end point levels in experiments 1 and 2

80x71mm (600 x 600 DPI)

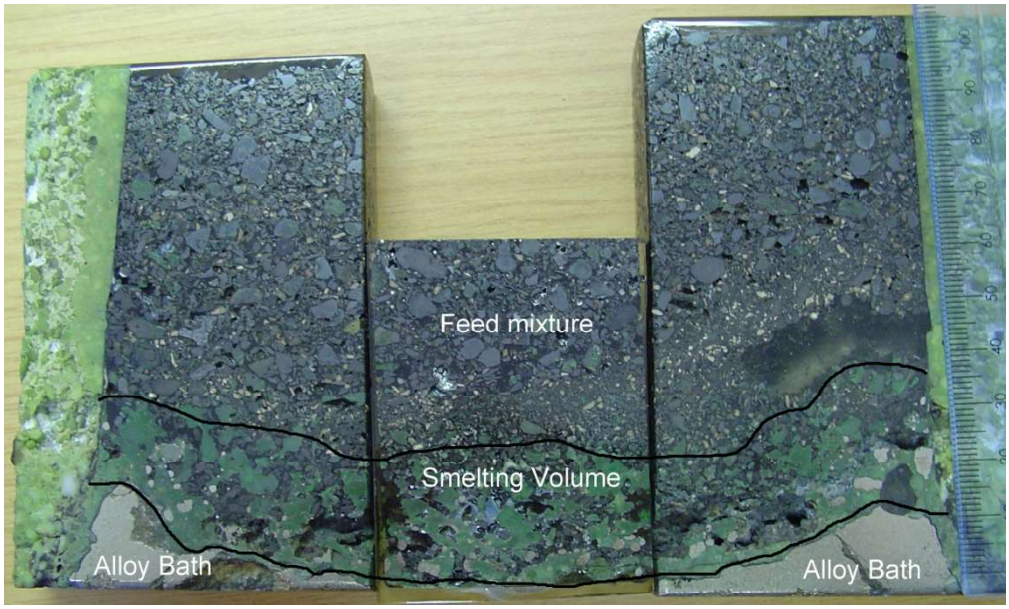

Figure 16: Reacted crucible content cross section

79x48mm (600 x 600 DPI)

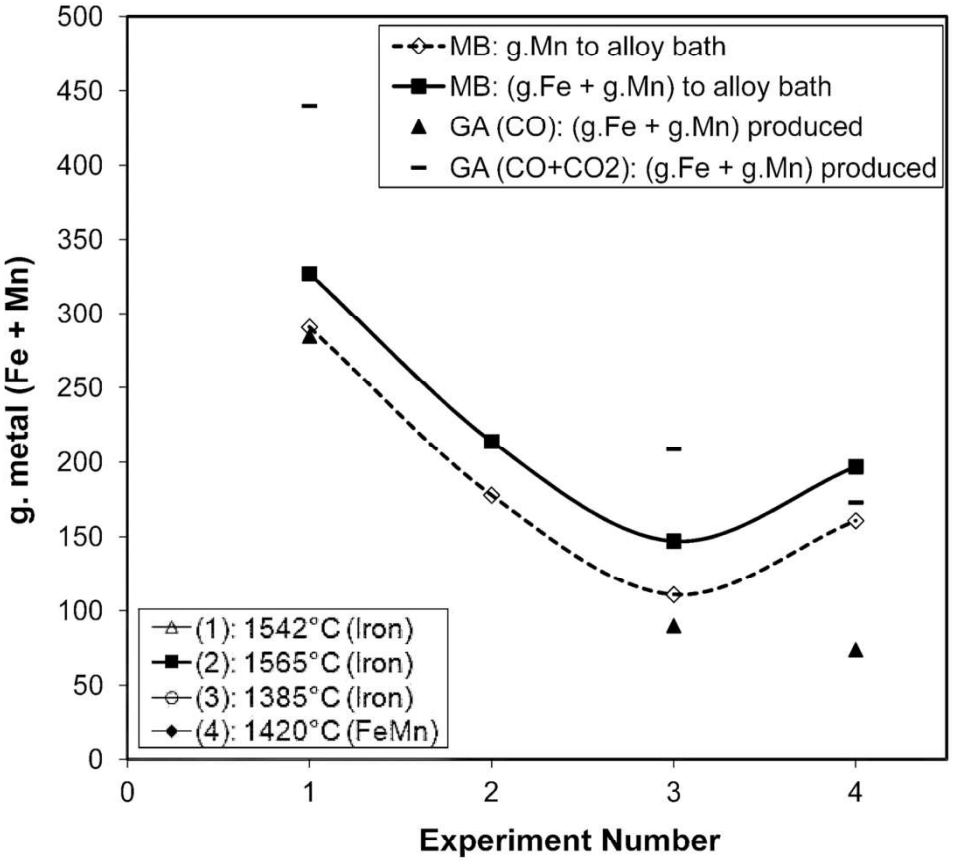

Figure 17: Metal mass produced: Mass balance (MB) vs. Gas analysis (GA)

80x71mm (600 x 600 DPI)